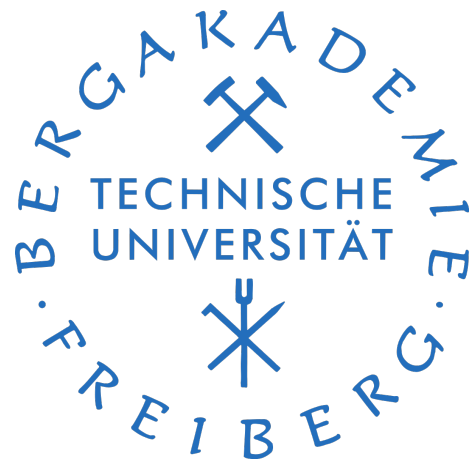


# **Development and implementation of material subroutine for fibre reinforced plastics in a commercial FEM software**

**Master thesis**

**Winter semester 2018/19**



Presented by: Arun prakash Ganapathy

Supervised by: Dr.-Ing Dominik Laveuve

Mat.Nr: 63876

E-mail: arun-prakash.ganapathy@student.tu-freiberg.de



# Contents

<b>1</b>	<b>Introduction</b>	<b>9</b>
1.1	Background and motivation . . . . .	9
<b>2</b>	<b>Continuum damage mechanics</b>	<b>12</b>
2.1	Damage . . . . .	12
2.2	Representative Volume Element(RVE) . . . . .	13
2.3	Concept of Continuum damage mechanics (CDM) . . . . .	14
2.3.1	Modelling by Effective Area Reduction . . . . .	14
2.3.2	Modelling by variation of elastic modulus . . . . .	16
2.4	Mechanical representation of the damage state . . . . .	17
2.4.1	Scalar Damage Variable . . . . .	17
2.4.2	Vector damage variable . . . . .	17
2.4.3	Damage tensor of second order . . . . .	17
2.5	Effective Stress Tensors . . . . .	18
2.5.1	Effective Stress Tensor for Isotropic Damage . . . . .	18
2.5.2	Asymmetric Effective Stress Tensor for Anisotropic Damage . . . . .	19
2.5.3	Symmetrized Effective Stress Tensor for Anisotropic Damage (Murakami and Ohno 1981) . . . . .	19
2.6	Damage effect tensors . . . . .	19
2.7	Hypothesis of Strain Equivalence . . . . .	20
2.8	Hypothesis of strain energy equivalence . . . . .	21
2.9	Elastic Constitutive equation and Elastic modulus tensor of orthotropic material . . . . .	23
<b>3</b>	<b>Working environment</b>	<b>26</b>
3.1	Software tools required . . . . .	26
3.2	Programming the UMAT . . . . .	27
3.3	Compiling UMAT . . . . .	28
3.4	Creating FE model . . . . .	29
3.5	Testing UMAT . . . . .	30
3.6	PostProcessing . . . . .	31

<b>4 Progressive Failure analysis of Orthotropic composite materials</b>	<b>33</b>
4.1 Fibre-reinforced Composites . . . . .	33
4.2 Mechanisms of damage and failure in fibre reinforced composites . . . . .	33
4.2.1 Longitudinal failure . . . . .	34
4.2.2 Transverse failure . . . . .	34
4.3 Damage initiation criteria . . . . .	35
4.3.1 Maximum strain criteria . . . . .	35
4.3.2 Maximum stress criteria . . . . .	36
4.3.3 3D Hashin's quadratic strain criteria . . . . .	37
4.3.4 Modified Hashin's failure criterion . . . . .	38
4.4 Types of damage evolution . . . . .	38
4.4.1 Isotropic damage . . . . .	39
4.4.2 Anisotropic damage . . . . .	40
4.5 Localisation and Mesh Regularisation . . . . .	41
4.6 Numerical implementation of the damage model in ANSYS . . . . .	42
4.6.1 Strain based damage model . . . . .	42
4.6.2 Stress based damage model . . . . .	43
4.7 Schematic of UMAT implementation . . . . .	45
<b>5 Results and Discussion</b>	<b>47</b>
5.1 Modelling Linear elastic behaviour of orthotropic materials . . . . .	47
5.2 Damage behaviour at integration point level . . . . .	49
5.2.1 Uniaxial tension . . . . .	50
5.2.2 Biaxial tension . . . . .	55
5.2.3 Triaxial tension . . . . .	56
5.3 Representative structural examples . . . . .	57
5.3.1 Notched tensile specimen . . . . .	58
5.3.2 Compact Tension (CT) Specimen . . . . .	64
5.3.3 Plate with hole (3D) . . . . .	72

# List of Figures

1.1	Composite materials used in a Boeing 787 'Dreamliner' . . . . .	9
2.1	Scales of damage observation . . . . .	13
2.2	Effective area reduction due to microcracks . . . . .	15
2.3	Damage of bar under tensile load . . . . .	16
2.4	Surface element in RVE of a damaged material . . . . .	18
2.5	Hypothesis of strain equivalence . . . . .	21
2.6	Hypothesis of strain energy equivalence . . . . .	22
3.1	Usermat Interface . . . . .	28
3.2	Table (TB) commands . . . . .	30
3.3	Time history post processor window . . . . .	31
4.1	Fracture planes in FRP material . . . . .	35
4.2	Types of degradation behaviour in damaged composite materials . . . . .	39
5.1	Stress-Strain relation (ANSYS vs USERMAT) . . . . .	47
5.2	Contour plots of the stress components $\sigma_{xx}, \sigma_{yy}$ and $\sigma_{zz}$ of the bar obtained using ANSYS(Figures a,c,e on the left) and USERMAT(Figures b,d,f on the right) . . . . .	49
5.3	Evolution of stress for uniaxial tension test in 11 direction . . . . .	50
5.4	Evolution of damage components for uniaxial tension test in 11 direction	51
5.5	Influence of softening parameter $P$ in the damage evolution) . . . . .	51
5.6	Convergence issue: Residual norm of the stress vs No of Newton-raphson iterations . . . . .	52
5.7	Evolution of stress and damage components with stress-based damage initiation criteria under uniaxial tension . . . . .	53
5.8	Influence of element volume ( $V$ ) in the damage evolution . . . . .	54
5.9	The Strain components $\epsilon_{22}$ and $\epsilon_{33}$ computed using algorithmic(a) and numerical tangent stiffness(b) under uniaxial tension . . . . .	55
5.10	Evolution of stress(Figures a,c on the left) and corresponding damage(Figure b,d on the right) components under biaxial tension . . . . .	56
5.11	Evolution of stress(Figures a,c,e on the left) and corresponding(Figures b,d,f on the right) damage components under triaxial tension . . . . .	57

5.12 Specimen geometry and boundary conditions. Dimensions are given in mm. Displacement controlled loading $U_x$ is applied . . . . .	59
5.13 Considered meshes (h is the length of the element along fracture zone and n the total number of elements) . . . . .	60
5.14 Convergence study: Global force-displacement response for model with regularization(Figures a,c,e on the left) and without regularization(Figures b,d,f on the right) . . . . .	60
5.15 Convergence study for model with(Figure a,c,e) and without(b,d,f) regularization: Damage contour plots $d_1$ at the end of the loading . . . . .	62
5.16 Damage contour plots $d_2$ at the end of the loading (Loading in transverse direction) . . . . .	63
5.17 Comparison of force-displacement response in longitudinal and transverse direction for h=0.5mm discretization . . . . .	63
5.18 Specimen geometry and boundary conditions. Dimensions are given in mm. Displacement controlled loading $U_x$ is applied . . . . .	64
5.19 Considered meshes (h is the length of the element along fracture zone and n the total number of elements) . . . . .	65
5.20 Convergence study: Global force-displacement response for three different meshes . . . . .	66
5.21 Damage distributions at the end of loading in longitudinal direction: Damage contour plots $d_1$ and $d_2$ . . . . .	67
5.22 Damage distributions at the end of loading in transverse direction: Damage contour plots $d_1$ and $d_2$ (h = 0.5mm discretization) . . . . .	67
5.23 Comparison of force-displacement response in longitudinal and transverse direction for h=0.5mm discretization . . . . .	68
5.24 Comparison of force-displacement response for different shear co-efficient ( $\alpha$ ) (h=1mm discretization) . . . . .	68
5.25 Evolution of stress components during longitudinal tensile loading (h=1mm discretization) . . . . .	69
5.28 Damage distributions at the end of Longitudinal loading: Damage contour plots $d_2$ for different shear co-efficient ( $\alpha$ ) . . . . .	70
5.29 Evolution of stress components during transverse tensile loading (h=1mm discretization) . . . . .	71
5.30 Damage distributions at the end of transverse loading: Damage contour plots $d_1$ for different shear co-efficient ( $\alpha$ ) . . . . .	71
5.31 Specimen geometry and boundary conditions. Dimensions are given in mm. Displacement controlled loading $U_x$ is applied . . . . .	72
5.32 Finite element discretization used for 3D damage study . . . . .	73
5.33 Global force-displacement response for the longitudinal tensile loading . . . . .	73
5.34 Contour plots of the damage distribution $d_1$ , $d_2$ and $d_3$ at the end of longitudinal tensile loading . . . . .	75

5.34 Contour plots of the damage distribution $d_2$ and $d_3$ at the end of trans-	
verse tensile loading . . . . .	76
5.34 Contour plots of the damage distribution $d_2$ and $d_3$ at the end of trans-	
verse compressive loading . . . . .	77

# List of Tables

4.1	Maximum strain criterion . . . . .	36
4.2	Maximum stress criterion . . . . .	36
5.1	Material parameters(Integration point studies) . . . . .	48
5.2	Material parameters (Representative structural examples) . . . . .	58

# Chapter 1

## Introduction

### 1.1 Background and motivation

Composite materials are made of two or more dissimilar materials of different physical or chemical properties when combined, create a material with properties unlike the individual constituent materials. The earliest use of composite materials date back to 3400 B.C when Mesopotamians glued wood strips at different angles to create plywood. Another notable example is the bow made by Mongols during 1200 A.D, which is made from a combination of bamboo, wood, cattle tendons and silk bonded with natural resin. In the early, 1900s bakelite based composites were developed for its non-conductivity and heat resistant properties and widely used in industrial and consumer applications. Now a days advanced composite materials are widely used in structural design in various industries such as aerospace, automobile, marine, petrochemical etc., due to their superior properties over traditional engineering materials.

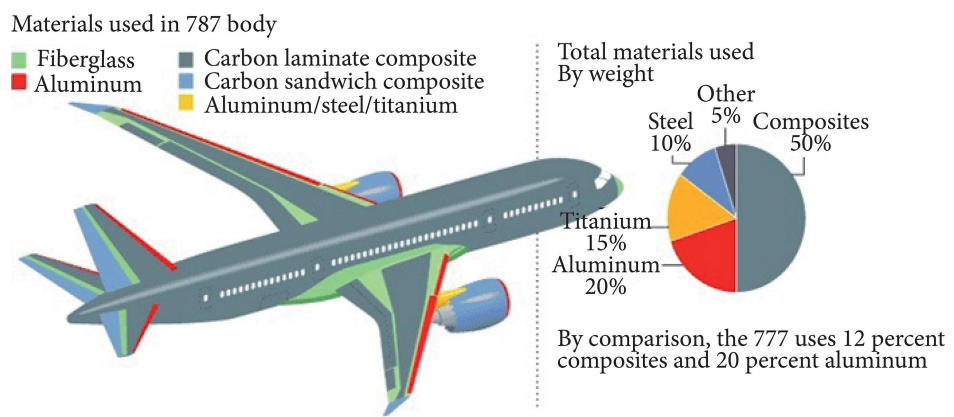


Figure 1.1: Composite materials used in a Boeing 787 'Dreamliner'

Composite material are attractive because of their high strength, stiffness, high stiffness-to-density ratio, light weight properties etc., Another important reason for using composite materials is the ability to tailor the stiffness and strength to specific

design load flexibly. Despite their superior physical properties, composite materials are fragile and can be easily damaged from number of sources, both during initial processing and in operation. Since composite materials possess elastic brittle properties with negligible margin of safety through ductility as offered by metals and accumulate damage before structural collapse, the development of damage must be understood for predicting failure of such materials. For example fibre-reinforced plastics exhibit local damage such as fibre breakage, matrix cracks, fibre matrix debonds etc., under normal operating conditions which may contribute to the failure. Therefore the ability to predict the initiation and growth of damage is important for predicting the performance of the composite materials for safe and reliable use of such materials. Continuum damage mechanics (CDM) has been considered as a reliable candidate for creating numerical models which predict the onset and evolution of the damage in the composite materials.



# Chapter 2

## Continuum damage mechanics

Continuum damage mechanics (CDM) is a theory for analyzing damage and fracture processes in materials from a continuum mechanics point of view. Continuum damage mechanics (CDM) provides a continuum perspective for microflaws initiation, propagation, and their coalescence that eventually results in macroscopic faults and fractures. CDM uses state variables to represent the damage effect on the stiffness and remaining life of the material that is damaging as a result of load and ageing. A Damage activation function is required to predict the initiation of damage. Damage evolution does not progress spontaneously after initiation therefore, a mathematical model is required.

### 2.1 Damage

Consider a body B of Fig. 2.1 where a crack of length  $a$  has developed due to an external load  $F$ . If we take an arbitrary point  $P(x)$  near the crack tip, a number of microscopic cavities or microcracks would be observed around the region. These cavities are usually developed due to breakage of atomic bonds, or some defects in the atomic array. From the microscopic point of view, fracture of materials is a process of nucleation of microcavities or microcracks due to the breakage of atomic bonds. From the macroscopic point of view, it is a process of extension of cracks brought about by the coalescence of these microcracks.

From the mesoscopic point of view, which exists between microscopic and macroscopic scale, it is a process of nucleation, growth and the coalescence of microscopic cavities that leads to the initiation of macroscopic crack. The development of microscopic, mesoscopic and macroscopic processes of fracture in materials and the resulting deterioration in their mechanical properties is called damage. Continuum damage mechanics aims to analyse the damage development during mesoscopic and macroscopic fracture processes in the framework of continuum mechanics.

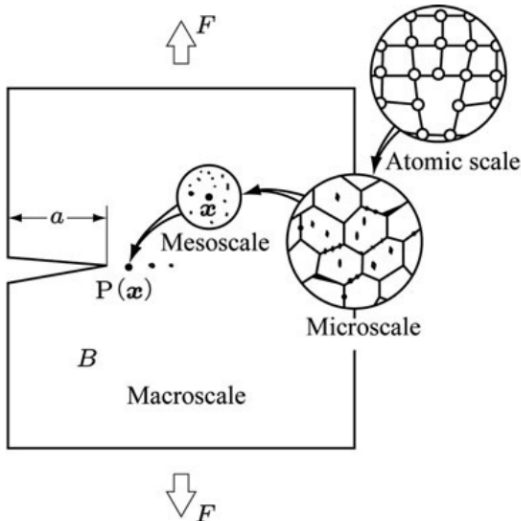


Figure 2.1: Scales of damage observation

The separation of atomic bonds is caused either by shear or tensile decohesion. However, the separation of material at the microscopic level consists of four damage mechanisms, namely Cleavage, Growth and Coalescence of Microvoids, Glide plane decohesion and Void Growth due to Grain-Boundary diffusion. The aspects of damage vary largely by the difference in materials and loading conditions. The damage may be classified phenomenologically as follows

- Ductile Damage
- Brittle Damage
- Creep Damage
- Low Cycle Fatigue
- Very Low Cycle Fatigue
- High Cycle fatigue damage
- Very High Cycle fatigue damage
- Creep Damage

## 2.2 Representative Volume Element(RVE)

To discuss the effects of microscopic discontinuities in a material using CDM we must homogenize the mechanical effects of microstructure and represent them as a macroscopic continuous field in the material. For this purpose, we take a small region

of a mesoscale around the material point  $P(x)$  in body B, as shown in Figure. 2.1. We assume that the material with discontinuous structures in this region as homogeneous, and the mechanical state of the material in this region can be represented by the statistical average of the mechanical variables in that region. This region is said to be the Representative Volume Element(RVE). For such RVE, the following two conditions must be satisfied:

- For the material in the RVE to be statistically homogeneous, the RVE should be large enough to contain a sufficient number of discontinuities
- To represent a non-uniform macroscopic mechanical field by means of a continuum, the size of RVE should be sufficiently small so that the variation of the macroscopic variable in it may be insignificantly small

The size of RVE depends on the microstructure of the relevant material and their typical sizes are as follows

- Metals and ceramics -  $0.1mm^3$
- Polymer and composites -  $1mm^3$
- Timber -  $10mm^3$
- Concrete -  $100mm^3$

## 2.3 Concept of Continuum damage mechanics (CDM)

The basic concept of CDM is that a set of damage variables can represent the microstructural defects in a material. Continuum damage mechanics first represent the damage state of a material in terms of damage variables and then describe the mechanical behaviour of the damaged material and then development of damage by use of these damage variables. The mechanical behaviour of a damaged material can be described using the notion of effective stress, together with the hypothesis of mechanical equivalence between damaged and undamaged material. The concept of effective stress and mechanical equivalence will be discussed in the following sections.

### 2.3.1 Modelling by Effective Area Reduction

Let us consider body B of Fig. (2.2) and take an RVE at an arbitrary point  $P(x)$  in B. If the total void area in  $dA$  is  $dA_D$ , the mechanical effect of  $dA$  will be decreased by  $dA_D$ . Then the area,

$$d\tilde{A} = dA - dA_D \quad (2.1)$$

maybe interpreted as the area which carries the internal force and is called as an *effective area*. Thus the damage variable D can be specified as

$$D = \frac{dA - d\tilde{A}}{dA} = \frac{dA_D}{dA} \quad (2.2)$$

where the damage variable  $D$  takes a value between 0 and 1 ( $0 \leq D \leq 1$ ).  $D = 0$  representing initial undamaged state and  $D = 1$  represents fully damaged state. Suppose a cylindrical bar of cross-sectional area  $dA$  is subject to a tensile load  $dF$  the

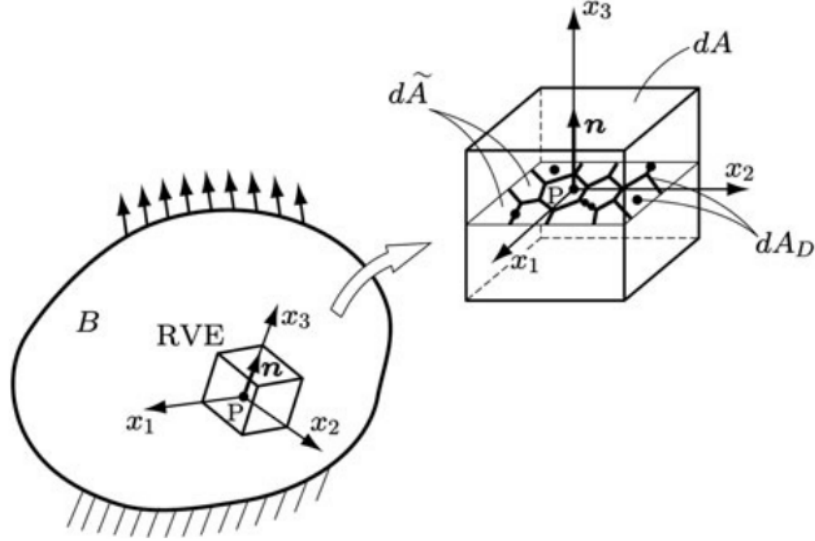


Figure 2.2: Effective area reduction due to microcracks

actual load carrying area is  $d\tilde{A}$  rather than  $dA$ . According to eqn (2.1) and (2.2) the effective area  $d\tilde{A}$  is given by,

$$d\tilde{A} = (1 - D)dA \quad (2.3)$$

The decrease in the load-carrying area increases the effect of stress  $\sigma$  induced by the external force  $dF$ . Due to eqn 2.3, the magnified stress  $\tilde{\sigma}$  is given by,

$$\tilde{\sigma} = \frac{dF}{d\tilde{A}} = \frac{\sigma}{1 - D} \quad (2.4)$$

Since the stress  $\tilde{\sigma}$  represents the effect of stress magnified by the net area reduction due to damage, it is called *effective stress*. From eqn (2.3) and (2.4) we can postulate that the damaged cylindrical bar of Fig.(2.3b) with the cross-sectional area  $dA$  subject to force  $dF$  is mechanically equivalent to the fictitious undamaged bar of Fig.(2.3c), which is subject to force  $dF$ , has the cross-sectional area  $d\tilde{A}$  and hence stress has the stress  $\tilde{\sigma}$

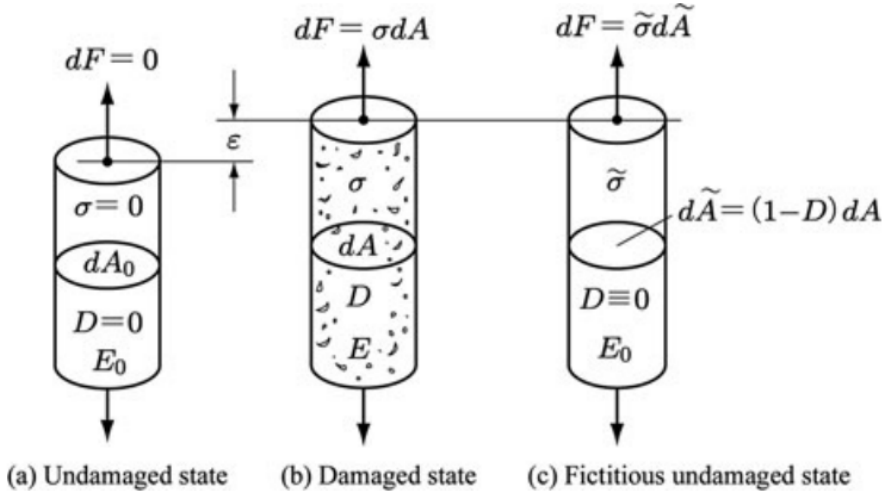


Figure 2.3: Damage of bar under tensile load

### 2.3.2 Modelling by variation of elastic modulus

Since the development of microcavities causes the reduction in material stiffness, the damage state can be characterized by variation in elastic modulus. Let us consider the bar (b) and (c) of Figure. (2.3) are in the damaged and fictitious undamaged state respectively. Then the elastic strain  $\epsilon$  in the bar (c) caused by stress  $\tilde{\sigma}$  should be equal to the  $\epsilon$  of the bar (b) under stress  $\sigma$ ; i.e.,

$$\tilde{\sigma} = E_0\epsilon, \quad \sigma = E(D)\epsilon \quad (2.5)$$

$$\epsilon = \frac{\sigma}{E(D)} = \frac{\tilde{\sigma}}{E_0} \quad (2.6)$$

where  $E_0$  and  $E(D)$  are the young's modulus of the material in the initial undamaged state and in damaged state after loading, respectively. Therefore, eqn. (2.6) defines another effective stress

$$\epsilon = \frac{E_0}{E(D)}\sigma \quad (2.7)$$

By combining Eqn. (2.4) and (2.6) we get,

$$E(D) = (1 - D)E_0 \quad (2.8)$$

$$D = 1 - \frac{E(D)}{E_0} \quad (2.9)$$

Therefore, the damage variable  $D$  is characterized by the variation in Young's modulus  $E(D)$ . The modelling of damage by means of reduction in stiffness can be applied also

the anisotropic damage of brittle materials like composite materials, concrete, rocks etc.,

## 2.4 Mechanical representation of the damage state

The deformation of material depends on the direction of applied stress or strain, and hence it is an anisotropic phenomena. Therefore different theories have been developed for modelling 3-D anisotropic damage phenomenon. Some fundamental theories that describe 3-D damage state are given below

### 2.4.1 Scalar Damage Variable

In the case of random or isotropic distribution of microcracks or voids, and when void density is small, the global mechanical properties can be approximated as nearly isotropic. The damage state, in this case, may be represented using scalar damage variable  $D$ . Thus isotropic damage theory based on isotropic damage variable has been often applied to 3-D problems of creep, elastic-plastic, ductile and fatigue damage

### 2.4.2 Vector damage variable

The damage state can be specified by the decrease in load carrying effective area due to void development. Hence it is easy to postulate a vector damage variable. Kachanov (1974, 1986) tried to extend the definition of damage to anisotropic damage by noting a surface element in an arbitrary direction  $n$ , he proposed vector damage variable  $\omega = \omega_n n$ , where  $\omega_n$  is the effective area fraction.

### 2.4.3 Damage tensor of second order

To describe an anisotropic damage state, damage variable of second or higher order tensor is required. Eqn.(2.3) suggests that the damage state  $(1 - D)$  is specified by the transformation of the surface element  $dA$  of Fig. (2.3b) of the damage state into the corresponding surface element  $d\tilde{A}$  in the fictitious undamaged state of Fig.(2.3c).

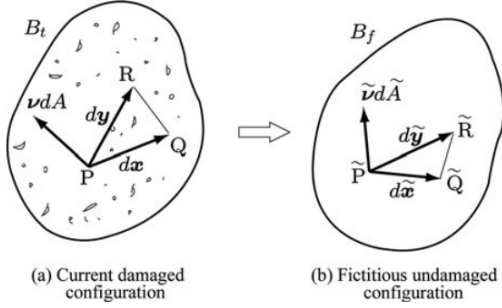


Figure 2.4: Surface element in RVE of a damaged material

To express damage as a second order tensor, we first consider an arbitrary surface element  $PQR$  in RVE in the current damaged configuration  $B_t$  of Fig.(2.4a) . The unit normal vector and area of  $PQR$  are denoted by  $\nu$  and  $dA$ . We further postulate the fictitious undamaged configuration  $B_f$  of Fig.(2.4b) mechanically equivalent to  $B_t$ , and the surface element and its area vector are denoted by  $\tilde{P}\tilde{Q}\tilde{R}$  and  $\tilde{\nu}d\tilde{A}$  respectively. According to Eqn.(2.3) the damage variable of second-order tensor  $D$  should be defined by linear transformation from area vector  $\nu dA$  in  $B_t$  into  $\tilde{\nu}d\tilde{A}$  in  $B_f$ , i.e.,

$$\tilde{\nu}d\tilde{A} = (I - D)\nu dA \quad (2.10)$$

where  $I$  is the second order identity tensor. Since the damage tensor  $D$  is symmetric, it can be expressed by its spectral decomposition

$$D = \sum_{i=1}^3 D_i n_i \otimes D_i n_i \quad (2.11)$$

where  $D_i$  and  $n_i$  are the principal value and principal direction of  $D$ .

## 2.5 Effective Stress Tensors

The effective stresses are used to describe the mechanical behaviour of the damaged material. Some of the effective stresses postulated in damage mechanics are given below

### 2.5.1 Effective Stress Tensor for Isotropic Damage

If the damage state is isotropic then the effective stress tensor of three-dimensional state is given by

$$\tilde{\sigma} = (1 - D)^{-1} \sigma \quad (2.12)$$

where  $D$  is the scalar damage variable, and  $\sigma$  is the Cauchy stress tensor. This effective stress simplifies damage theory and can be applied to a number of damage problems

like ductile damage. But this cannot be applied to damage of significant anisotropy, such as brittle damage due to microcrack distribution.

### 2.5.2 Asymmetric Effective Stress Tensor for Anisotropic Damage

The increase in stress effect caused by the net area reduction in case of anisotropic damage is given by

$$\tilde{\sigma} = (I - D)^{-1} \sigma \quad (2.13)$$

where  $I$  and  $D$  are second-order identity tensor and the second-order damage tensor, respectively. In the actual development of anisotropic damage, the stress-induced in RVE of damage material is asymmetric. But asymmetric stress tensor makes the numerical analysis complicated, and thus different methods of symmetrization have been proposed. Few of them are described as follows

### 2.5.3 Symmetrized Effective Stress Tensor for Anisotropic Damage (Murakami and Ohno 1981)

A simple symmetrization procedure of Eq.(2.14), the symmetric part of the Cartesian decomposition of Eq.(2.14) gives,

$$\tilde{\sigma} = \frac{1}{2}[(I - D)^{-1} \sigma + \sigma(I - D)^{-1}] \quad (2.14)$$

## 2.6 Damage effect tensors

The general form of an effective stress tensor  $\tilde{\sigma}$  is given by the damage effect tensor  $\mathbb{M}$  and the corresponding Cauchy stress tensor  $\sigma$ , i.e.,

$$\tilde{\sigma} = \mathbb{M} : \sigma \quad (2.15)$$

It is convenient to express the tensors in the form of matrices and then execute the tensor operations as a matrix calculus.. To simplify this procedure, we take an orthonormal basis  $n_i$  with principal directions  $n_i$  of the second-order symmetric damage tensor  $D$ , and represent the tensor in terms of their component to this basis. According to voigt notation, the second-order symmetric tensor  $\sigma$  and the related effective stress  $\tilde{\sigma}$  are expressed by the column vector of six dimension:

$$[\sigma_P] \equiv [\sigma_{11} \ \sigma_{22} \ \sigma_{33} \ \sigma_{12} \ \sigma_{13} \ \sigma_{23}]^T \quad (2.16)$$

$$[\tilde{\sigma}_P] \equiv [\tilde{\sigma}_{11} \ \tilde{\sigma}_{22} \ \tilde{\sigma}_{33} \ \tilde{\sigma}_{12} \ \tilde{\sigma}_{13} \ \tilde{\sigma}_{23}]^T \quad (2.17)$$

By means of the matrix representation, we have the matrix form

$$[\tilde{\sigma}_P] \equiv [\mathbb{M}_{pq}] : [\sigma_P] \quad (2.18)$$

Matrix representation of the damage effect tensor of Eq.(2.18) is shown below

$$[\mathbb{M}_{pq}] \equiv \begin{bmatrix} \frac{1}{\omega_{11}} & 0 & 0 & 0 & 0 & 0 \\ 0 & \frac{1}{\omega_{22}} & 0 & 0 & 0 & 0 \\ 0 & 0 & \frac{1}{\omega_{33}} & 0 & 0 & 0 \\ 0 & 0 & 0 & \frac{1}{\omega_{12}} & 0 & 0 \\ 0 & 0 & 0 & 0 & \frac{1}{\omega_{23}} & 0 \\ 0 & 0 & 0 & 0 & 0 & \frac{1}{\omega_{13}} \end{bmatrix}$$

where

$$\omega_{11} = (1 - d_1) \quad \omega_{22} = (1 - d_2) \quad \omega_{33} = (1 - d_3)$$

$$\omega_{12} = \sqrt{(1 - d_1)(1 - d_2)} \quad \omega_{23} = \sqrt{(1 - d_2)(1 - d_3)} \quad \omega_{13} = \sqrt{(1 - d_1)(1 - d_3)}$$

## 2.7 Hypothesis of Strain Equivalence

The inelastic constitutive equation of a damaged material is given by the corresponding constitutive equation for an undamaged material by replacing the stress tensor  $\sigma$  in the equation with the corresponding effective stress tensor  $\tilde{\sigma}$ . In Fig. the effect of stress  $\sigma$  acting on RVE in the current damaged configuration  $B_t$  is equivalent to that of the stress  $\tilde{\sigma}$  in the fictitious undamaged configuration. Therefore the deformation of the damaged material subject to stress  $\sigma$  should be equal to that of the fictitious undamaged material subject to stress  $\tilde{\sigma}$ . Suppose the constitutive equation of an undamaged inelastic material is given by

$$\epsilon = F_0(\sigma, \alpha) \quad (2.19)$$

or

$$\dot{\epsilon} = F_0(\sigma, \alpha) \quad (2.20)$$

where  $\alpha$  is an internal variable representing the internal change other than damage. and  $(\cdot)$  denotes the material time derivative

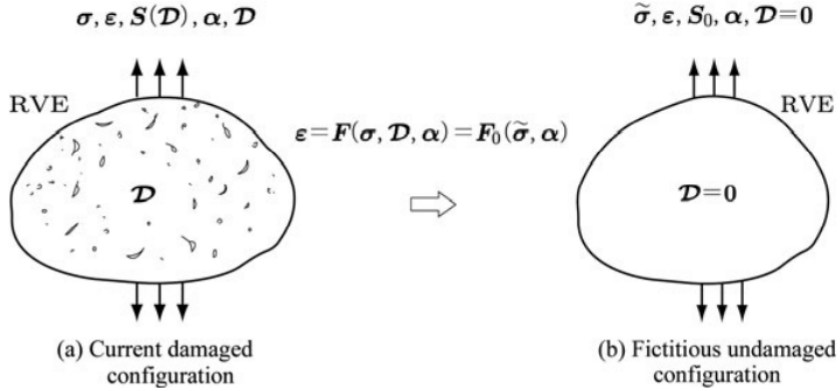


Figure 2.5: Hypothesis of strain equivalence

Then according to hypothesis of strain equivalence, the inelastic constitutive equation of the damaged material represented by a damage variable  $D$  should be given by replacing  $\sigma$  of Eq.(25) with the effective stress  $\tilde{\sigma}$  i.e.,

$$\epsilon = F(\sigma, D, \alpha) = F_0(\tilde{\sigma}, \alpha) \quad (2.21)$$

or

$$\dot{\epsilon} = F(\sigma, D, \alpha) = F_0(\tilde{\sigma}, \alpha) \quad (2.22)$$

In case of elastic deformation, constitutive equations for an undamaged and damaged material is given by

$$\epsilon = \mathbb{S}_0 : \sigma, \quad (2.23)$$

$$\epsilon = \mathbb{S}(D) : \sigma, \quad (2.24)$$

where  $\mathbb{S}_0$  and  $\mathbb{S}(D)$  are fourth-order elastic compliance tensors of the materials. Therefore, according to the hypothesis of strain equivalence the elastic constitutive equation of the damaged material and the compliance tensor is given by

$$\epsilon = \mathbb{S}_0 : \tilde{\sigma} = [\mathbb{S}_0 : \mathbb{M}(D)] : \sigma = \mathbb{S}(D) : \sigma \quad (2.25)$$

$$\mathbb{S}(D) = \mathbb{S}_0 : \mathbb{M}(D) \quad (2.26)$$

where  $\mathbb{M}(D)$  is the damage effect tensor which is given by

$$\mathbb{M}(D) = \mathbb{S}_0^{-1} : \mathbb{S}(D) \quad (2.27)$$

## 2.8 Hypothesis of strain energy equivalence

The existence of strain energy function necessitates the symmetry of the compliance and elastic modulus tensor. But the compliance tensor resulting from hypothesis

of strain equivalence is asymmetric which does not satisfy the requirement. Therefore hypothesis of strain energy equivalence is used to satisfy the symmetry requirements. Let us consider an elastic-plastic material and represent the internal change due to plastic deformation by an internal state variable  $\alpha$ . The complementary strain energy functions of the material at undamaged and damaged state are given, respectively as follows

$$V_0(\sigma, \alpha) = \frac{1}{2}\sigma : \mathbb{S}_0 : \sigma - \phi(\alpha) \quad (2.28)$$

$$V(\sigma, D, \alpha) = \frac{1}{2}\sigma : \mathbb{S}(D) : \sigma - \phi(\alpha) \quad (2.29)$$

Thus the constitutive equation for the undamaged and damaged material

$$\epsilon = \frac{\partial V_0}{\partial \sigma} = \mathbb{S}_0 : \sigma \quad (2.30)$$

$$\epsilon = \frac{\partial V}{\partial \sigma} = \mathbb{S}(D) : \sigma \quad (2.31)$$

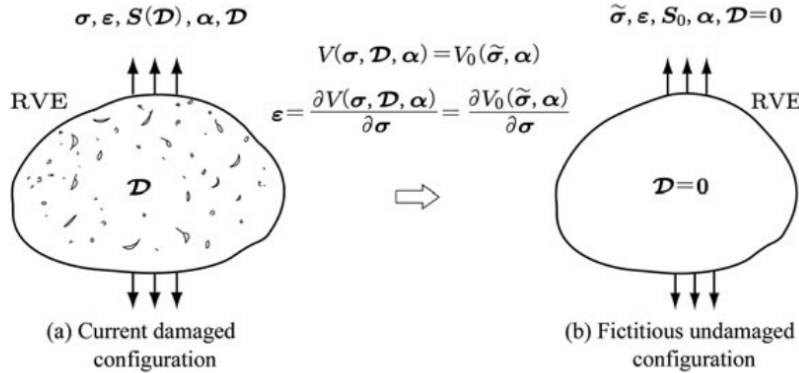


Figure 2.6: Hypothesis of strain energy equivalence

Suppose a damaged material of Fig.(2.6)a subject to stress  $\sigma$ , and represent the damage and internal state due to inelastic deformation by  $D$  and  $\alpha$ , respectively. Then the strain energy function  $V(\sigma, D, \alpha)$  of the damaged material is given by replacing  $\sigma$  in the corresponding function  $V_0(\sigma, \alpha)$  of the undamaged material of Fig.(2.6)b with effective stress  $\tilde{\sigma}$

$$V(\sigma, D, \alpha) = V_0(\tilde{\sigma}, \alpha)$$

By the use of this hypothesis, the elastic strain of Eq.(2.31) leads to

$$\begin{aligned}
\epsilon &= \frac{\partial V(\sigma, D, \alpha)}{\partial \sigma} = \mathbb{S}(D) : \sigma \\
&= \frac{\partial V_0(\tilde{\sigma}, \alpha)}{\partial \sigma} = \frac{\partial}{\partial \sigma} \left( \frac{1}{2} \tilde{\sigma} : \mathbb{S}_0 : \tilde{\sigma} \right) \\
&= \frac{1}{2} \frac{\partial}{\partial \sigma} [(\mathbb{M}(D) : \sigma) : \mathbb{S}_0 : (\mathbb{M}(D) : \sigma)] \\
&= [\mathbb{M}^T(D) : \mathbb{S}_0 : \mathbb{M}(D)] \tag{2.32}
\end{aligned}$$

From Eq.(2.32), the elastic compliance tensor of the damaged material is given as follows

$$\mathbb{S}(D) = \mathbb{M}^T(D) : \mathbb{S}_0 : \mathbb{M}(D) \tag{2.33}$$

If the damage effect tensor  $\mathbb{M}(D)$  can be expressed as a fourth-order symmetric tensor, then the elastic compliance tensor  $\mathbb{S}(D)$  becomes fourth-order symmetric tensor which satisfies the thermodynamic requirement.

## 2.9 Elastic Constitutive equation and Elastic modulus tensor of orthotropic material

Orthotropic materials are materials that exhibit different material properties along three mutually orthogonal axis. They are a special form of anisotropic materials because their properties change when measured from different directions. Some examples of orthotropic materials are wood, composite materials etc., Orthotropic materials require 9 independent variables to express their constitutive matrix. The 9 elastic constants are three Young's moduli  $E_x, E_y, E_z$ , the three Poisson's ratios  $\nu_{xy}, \nu_{yz}, \nu_{zx}$ , and three shear moduli  $G_{xy}, G_{yz}, G_{zx}$ . The elastic stiffness matrix of orthotropic material has the form,

$$\sigma = \mathbb{C}_0 : \epsilon \quad or \quad \sigma_{ij} = C_{ijkl}^0 \epsilon_{kl}, \tag{2.34}$$

$$[C_{pq}^0] = \begin{bmatrix} \frac{1-\nu_{yz}\nu_{zy}}{E_y E_z \Delta} & \frac{\nu_{xy}+\nu_{xz}\nu_{zy}}{E_y E_z \Delta} & \frac{\nu_{xz}+\nu_{xy}\nu_{yz}}{E_y E_z \Delta} & 0 & 0 & 0 \\ \frac{\nu_{yx}+\nu_{yz}\nu_{zx}}{E_x E_z \Delta} & \frac{1-\nu_{xz}\nu_{zx}}{E_1 E_z \Delta} & \frac{\nu_{yz}+\nu_{yx}\nu_{xz}}{E_1 E_z \Delta} & 0 & 0 & 0 \\ \frac{\nu_{zx}+\nu_{yx}\nu_{zy}}{E_x E_y \Delta} & \frac{\nu_{zy}+\nu_{xy}\nu_{zx}}{E_x E_y \Delta} & \frac{1-\nu_{xy}\nu_{yx}}{E_x E_y \Delta} & 0 & 0 & 0 \\ 0 & \nu & \nu & G_{xy} & 0 & 0 \\ 0 & \nu & \nu & 0 & G_{yz} & 0 \\ 0 & \nu & \nu & 0 & 0 & G_{zx} \end{bmatrix}$$

where

$$\Delta = (1 - \nu_{xy}\nu_{yx} - \nu_{yz}\nu_{zy} - \nu_{zx}\nu_{xz} - 2\nu_{xy}\nu_{yz}\nu_{zx}) / E_x E_y E_z$$

and  $\frac{\nu_{xy}}{E_y} = \frac{\nu_{yx}}{E_x}$ ,  $\frac{\nu_{yz}}{E_z} = \frac{\nu_{zy}}{E_y}$ ,  $\frac{\nu_{xz}}{E_z} = \frac{\nu_{zx}}{E_x}$



# Chapter 3

## Working environment

The material models necessary for simulating progressive damage must be programmed first using a programming language, compiled, and then tested in a commercial FEM software. The programming language of choice for most commercial FEM software is FORTRAN because they are fast and straightforward. To program the material model, an integrated development environment (IDE) and a compiler compatible with the version of the FEM software are required. This chapter describes the necessary tools for creating material models and how to use them to test the models in detail.

### 3.1 Software tools required

- **OCTAVE**

Octave is an open-source version of programming language software MATLAB. Initially, the user material subroutines are developed on Octave and tested using simple tests like uniaxial tension with the help of constitutive driver routines

- **Visual studio**

Visual Studio is the IDE used for programming and debugging user material subroutines using the FORTRAN programming language.

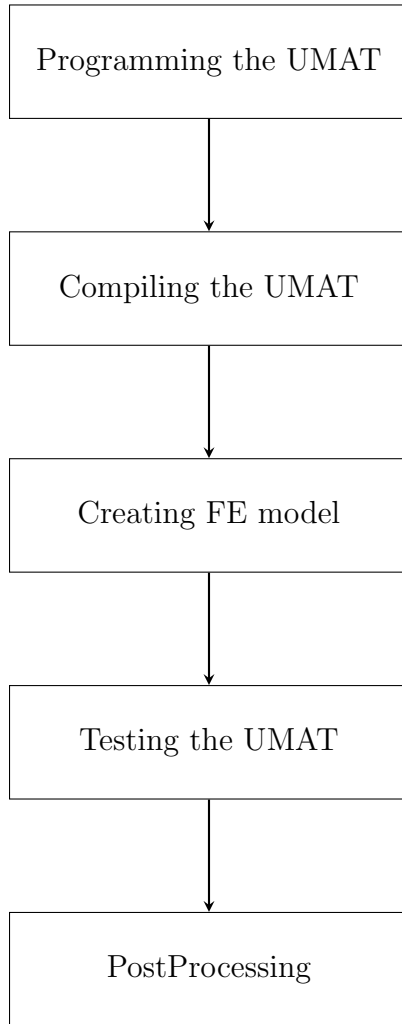
- **Intel parallel studio**

The compiler available in Intel parallel studio is used for compiling the material subroutines before testing them in a FEM software.

- **ANSYS**

ANSYS is the commercial FEM software chosen for creating specimens and analyzing how the material models behave in different test conditions

The following sections provide the reader with a detailed description, starting from developing the user-defined material subroutine to implementing and analysing the results in the ANSYS environment. The flowchart below shows the steps involved in the whole process



### 3.2 Programming the UMAT

The user material subroutine is an ANSYS programmable feature which allows user to write their own material constitutive equations with in a newly developed general material framework. The subroutine is called at all material integration points of the element during the solution phase.

ANSYS demands the necessary variables declared in a certain way so that the USERMAT developed can work compatibly with ANSYS when it is called at each integration point. The guidelines for declaring input and output arguments can be found on ANSYS' usermat guide. The following image shows the user subroutine

interface with the set of possible input arguments that USERMAT can access from ANSYS

For every Newton raphson iteration, the USERMAT is called at every material in-

```

subroutine usermat(
&           matId, elemId,kDomIntPt, kLayer, kSectPt,
&           ldstep,isubst,keycut,
&           nDirect,nShear,ncomp,nStatev,nProp,
&           Time,dTime,Temp,dTemp,
&           stress,statev,dsdePl,sedEl,sedPl,epseq,
&           Strain,dStrain,epsPl,prop,coords,
&           tsstif, epsZZ,
&           var1, var2, var3, var4, var5,
&           var6, var7, var8)

      INTEGER
&           matId, elemId,
&           kDomIntPt, kLayer, kSectPt,
&           ldstep,isubst,keycut,
&           nDirect,nShear,ncomp,nStatev,nProp
      DOUBLE PRECISION
&           Time,     dTime,     Temp,     dTemp,
&           sedEl,    sedPl,    epseq,    epsZZ
      DOUBLE PRECISION
&           stress  (ncomp ), statev  (nStatev),
&           dsdePl (ncomp,ncomp),
&           Strain (ncomp ), dStrain (ncomp ),
&           epsPl  (ncomp ), prop     (nProp ),
&           coords (3),      rotateM (3,3),
&           defGrad_t(3,3),   defGrad(3,3),
&           tsstif  (2)

```

Figure 3.1: Usermat Interface

tegration point, and the ANSYS passes in strains, stresses and state variables at the beginning of the time increment and the current strain increment. The USERMAT then has to compute and update the necessary output arguments like stresses and state variables at the end of the increment and the material tangent stiffness matrix  $\frac{\partial\sigma}{\partial\epsilon}$ .

### 3.3 Compiling UMAT

The user-programmable subroutines must be compiled before testing them in ANSYS environment. The compilation process first checks for errors in the source and then converts them into ANSYS executable files (.dll files), which can be used by ANSYS. The compiler present in Intel parallel studio is used for this purpose. The step by step process of compiling the UMAT is given below

- Create an empty directory and copy the usermat file you want to compile (.f files) into the empty directory.

- Change the name of your usermat file to *usermat*
- Go to "Control Panel>Search System>Edit the system environment variables>Environment variables" and click New in the user variables for your PC, which opens a window
- In that window, type ANS\_USER\_PATH for variable name and for variable value, copy and paste the path to your working directory and click Ok
- Go to folder "C:\ Program Files\ ANSYS Inc\ v181\ ansys\ custom\ user\ win64" and copy the ANSUSERSHARED.bat file and paste it in the working directory
- Open command prompt and navigate to the working directory
- Type ANSUSERSHARED.bat and press enter. This opens the Intel compiler and asks for user-programmable feature source file name
- Type *usermat* without extension and press Enter.
- If there is no error in the usermat file the compiler will show the message "usermatLib.dll has been successfully build."
- For the ANSYS to access these .dll files, open ANSYS Mechanical APDL product launcher and in the file management section browse to the current working directory
- Click run and in the Mechanical APDL output window you shoud see the message "Note - This ANSYS version was linked by Licensee". This indicates that you are using the shared library with the USERMAT

### 3.4 Creating FE model

The preprocessor section of the ANSYS mechanical APDL is used to create and mesh the FE model. The ANSYS user-programmable feature can be used with 18x family elements, which include LINK180, PLANE 182, PLANE 183, SOLID 185, SOLID 186. The type of element required for creating FE model based on the problem can be chosen from the element type menu in the preprocessor section. Once the element type is chosen, the material model, and the material properties can be entered in the *Material props* section. The *Modelling* section can be utilised to create the geometry required for testing the subroutines and then can be meshed using the *Meshing* option.

To use the FE model, again and again, to test different material models with different material properties the FE model can be saved in the form of an APDL script. An APDL script is a simple text file containing the command required to create

and solve the FE model. A simple way to create an APDL script for an FE model is to copy the log of commands automatically created in the log file during the creation of your model and pasting it a new text file. This log file can be accessed by going to *List > Files > Logfile*. The created APDL script can then be accessed by going to *File > Read input from* and navigate and select your file.

### 3.5 Testing UMAT

To use the user material option, the TB,USER command must be included in the APDL script so that the user material can be defined. The table command for USER material option is

**TB,USER,matId,NTEMPS,NPTS**

matId - material reference number

NTEMPS - Number of temperature points

NPTS - Number of material constants at a given temperature

If state variables are used in the subroutine, the number of state variables need to be defined in the APDL script by the command TB,STATE

**TB,STATE,matId,,NPTS**

matId - material reference number

NPTS - Number of state variables to be used in USERMAT

A simple example for defining user material and two state variables is given int the Fig.(3.2) below

```
!*
YOUNG = 210e3
POISSON = 0.33
T1 = 1

TB,USER,1,1,2,
TBTEMP,T1
TBDATA,,YOUNG,POISSON
TB,STATE,1,,2
```

Figure 3.2: Table (TB) commands

Before defining boundary conditions (BCs), the entities required for solving the FE model, such as time at the end of the load step, the number of steps, the results to be stored etc., must be defined. This can be done using *Sol'n Controls* option in the solution menu. Once the BCs are defined, the model can be solved by giving the command *SOLVE*.

### 3.6 PostProcessing

Once the FE model has finished solving, the results can be analyzed using the 'General Postprocessor' option. The nodal and elemental solution for components like stress, strain, displacement etc., can be plotted using the 'contour plot' option, which can be found on Plot results. By default, this option plots the results at the last substep, so to plot the solution at the substep of your choice one must navigate to *Read results > By pick* and select the substep to be plotted. Since the posprocessor of ANSYS does not have GUI option for plotting state variables the following command must be given: *plnsol, svar, n* where *n* is the number of the state variable to be plotted. The time history of a certain variable, such stress, reaction force, strain etc., at a node or an element can be plotted using *TimeHist Postpro* option. On clicking the *TimeHist Postpro* option a *Variable List* window opens up. To add the variables to plot, click the green add symbol on the top-left corner which opens a window with the list of variables that can be added to the *Variable List* window. Once the variables have been added, the variables can be plotted against each other or against time. Fig.(3.3) shows the *Variable List* window with X-component of force and displacement of node 3 selected and plotted against each other.

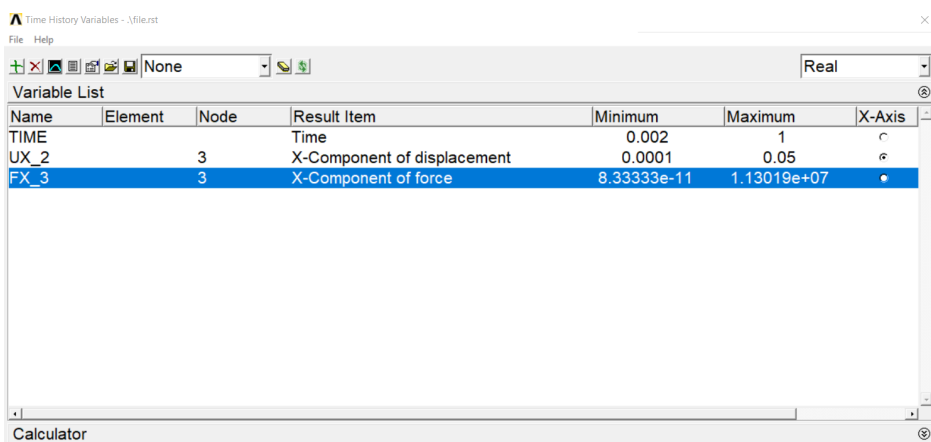


Figure 3.3: Time history post processor window

The time history results of each variable at node or an element can also be saved as text file using *List Data* option in the *Variable List* window.



# **Chapter 4**

## **Progressive Failure analysis of Orthotropic composite materials**

### **4.1 Fibre-reinforced Composites**

Fibre-reinforced plastic composites is a term for a large family of materials ranging from short fibre reinforced polyesters to unidirectional graphite fibre epoxies. Fibre-reinforced composites consist of three components 1) the fibres as the discontinuous or dispersed phase, 2) the matrix as the continuous phase, and 3) the fine interphase region, also known as the interface. The different combinations of fibre and matrix material lead to different material properties and the manifestation of the fibres and the manufacturing techniques. The first fibres used in fibre reinforced plastics are made of glass. Although the virgin strength of the glass is high, the actual strength is limited by the microscopic defects on the surface of the fibre. The graphite fibres are anisotropic due to their laminar structure. Graphite fibres maintain their strength even at high temperatures. Two types of plastics are commonly used as matrix materials, namely unsaturated polyesters and epoxies. The use of unsaturated polyesters is restricted to temperatures up to 100C. The main advantage of this material is the high amount of shrinkage at hardening, which causes high internal stress and decrease the strength of the material. The characteristics of epoxy are better than polyester resins. The material can withstand temperatures up to 250C and shrinks only 2% at hardening. However, epoxy resins are high in price compared to polyesters.

### **4.2 Mechanisms of damage and failure in fibre reinforced composites**

The failure in fibre reinforced composites happens mainly due to matrix cracking or fibre failure. Therefore the failure can be divided mainly two types, namely 1) Longitudinal failure and 2) Transverse failure. The mechanism of both failure mechanisms, their causes and their effects on material behaviour are discussed in detail

below

#### **4.2.1 Longitudinal failure**

In fibre-reinforced plastics, the most significant portion of the load is resisted by fibres. When the fibres fail, the load must redistribute to other areas of the structure and may cause structural collapse. In composites where strain to failure for resin matrix is higher than one of the reinforcing fibre, longitudinal failures start by isolated fibre fractures in weak zones. This kind of localized fracture increases the normal and interfacial shear stress in fibres and promotes matrix cracking, fibre matrix debonding, conical shear failures, etc. When the load is further increased, it may lead to the final collapse. Longitudinal tensile failure occurs in both constituents, and a fracture occurs along a plane whose normal is parallel to the fibre direction. Simple maximum stress or maximum strain can usually provide an accurate measure of longitudinal tensile failure. Longitudinal compressive failure occurs from the collapse of the fibres due to shear kinking and damage of the supporting matrix. Fibre misalignment causes shear stress between fibres that rotate fibres, which increases shear stress further and leads to instability.

#### **4.2.2 Transverse failure**

Transverse failure happens due to matrix cracking and fibre-matrix debonding. Under the presence of in-plane shear stress and transverse tensile stress, the combined effects of defects such as resin-rich regions, fibre-resin debonds, and resin voids trigger a transverse crack that extends through the thickness. The transverse cracks are formed at the fibre-resin interface without affecting the fibres. When a unidirectional fibre composite is loaded in shear, a non-linear shear stress-strain behaviour is observed before the material fails by through-thickness matrix cracking. This non-linear behaviour is due to the visco-plastic behaviour of the matrix and from the nucleation of microvoids.

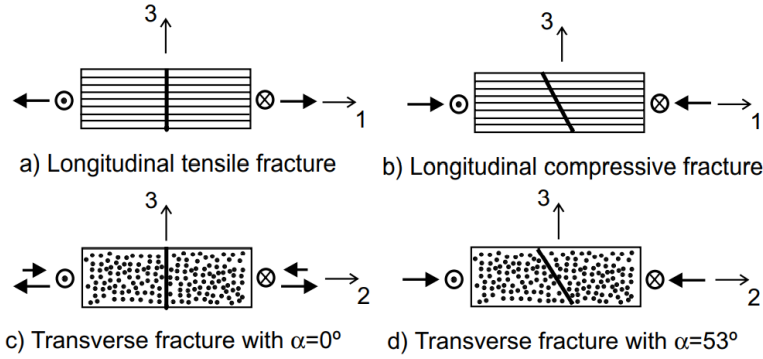


Figure 4.1: Fracture planes in FRP material

Experimental results have shown that moderate compression has beneficial effects on the strength of the material (Soden et al., 1998); when the transverse compressive stress value is smaller than the in-plane shear stress, the fracture plane is perpendicular to the mid-plane of the ply. Increasing the compressive stress changes angle of the fracture plane. For glass-epoxy and carbon-epoxy composites, when loaded in pure transverse compression, the fracture plane is at an angle of  $53^\circ \pm 3^\circ$  with respect to the thickness direction. Therefore, the matrix cracking does not occur in the plane of maximum transverse shear stress ( $45^\circ$ ).

### 4.3 Damage initiation criteria

Damage initiation criteria refer to the onset of damage at a material point. Since the properties of the orthotropic materials change in the mutually perpendicular direction, three failure mode indices,  $F_f$ ,  $F_m$ ,  $F_z$ , are used for failure modes in three principal material directions. Since the failure due to tension and compression in each direction cannot happen at the same integration point and at the same time, the failure mode index must be calculated based on whether the material direction is under tension or compression. Both strain and stress-based damage initiation criteria can be employed based on the application. Some of the damage initiation criteria are given as follows

#### 4.3.1 Maximum strain criteria

The maximum strain criterion is a simple criterion which checks whether the strain in the given material direction exceeds the failure strain or not. The maximum strain criterion for each material direction is given below

---

Damage direction	Tension	Compression
Fibre direction 1 ( $F_f$ )	$\frac{\epsilon_1}{\epsilon_{t1}} \leq 1$	$\frac{\epsilon_1}{\epsilon_{c1}} \leq 1$
Matrix direction 2 ( $F_m$ )	$\frac{\epsilon_2}{\epsilon_{t2}} \leq 1$	$\frac{\epsilon_2}{\epsilon_{c2}} \leq 1$
Matrix direction 3 ( $F_z$ )	$\frac{\epsilon_3}{\epsilon_{t3}} \leq 1$	$\frac{\epsilon_2}{\epsilon_{c3}} \leq 1$

---

Table 4.1: Maximum strain criterion

where  $\epsilon_{ti}$  and  $\epsilon_{ci}$  are failure strains in tension and compression respectively, in each material direction.

#### 4.3.2 Maximum stress criteria

Since the load-carrying area decreases due to an increase in damage, the effect of stress gets magnified in the damaged material. Therefore, in the case of maximum stress criteria, normal stress components of the effective stress( $\tilde{\sigma}$ ) are checked against the failure strength in each principal material direction. The effective stress can be computed using the Eqn.(2.15). The maximum stress criteria for each material direction is given in the table below

---

Damage direction	Tension	Compression
Longitudinal direction 1 ( $F_f$ )	$\frac{\tilde{\sigma}_{11}}{X_T} \leq 1$	$\frac{\tilde{\sigma}_{11}}{-X_C} \leq 1$
Transverse direction 2 ( $F_m$ )	$\frac{\tilde{\sigma}_{22}}{Y_T} \leq 1$	$\frac{\tilde{\sigma}_{22}}{-Y_C} \leq 1$
Transverse direction 3 ( $F_z$ )	$\frac{\tilde{\sigma}_{33}}{Z_T} \leq 1$	$\frac{\tilde{\sigma}_{33}}{-Z_C} \leq 1$

---

Table 4.2: Maximum stress criterion

where  $X_T, Y_T$  and  $Z_T$  are failure strength in tension and  $X_C, Y_C$  and  $Z_C$  are failure strength in compression in each principal material direction respectively.

#### 4.3.3 3D Hashin's quadratic strain criteria

Hashin's quadratic strain criteria includes shear strain components in addition to the normal strain components. The criteria for each material direction is given below

i) Longitudinal direction 1 ,

$$F_f^2 = \begin{cases} \left(\frac{\epsilon_{11}}{\epsilon_{11}^{f,t}}\right)^2 + \left(\frac{\epsilon_{12}}{\epsilon_{12}^f}\right)^2 + \left(\frac{\epsilon_{13}}{\epsilon_{13}^f}\right)^2 \geq 1 & (\epsilon_{11} > 0) \\ \left(\frac{\epsilon_{11}}{\epsilon_{11}^{f,c}}\right)^2 \geq 1 & (\epsilon_{11} < 0) \end{cases} \quad (4.1)$$

ii) Transverse direction 2,

$$F_m^2 = \begin{cases} \frac{(\epsilon_{22}+\epsilon_{33})^2}{\epsilon_{22}^{f,t}\epsilon_{33}^{f,t}} - \frac{\epsilon_{22}\epsilon_{33}}{(\epsilon_{23}^f)^2} + \left(\frac{\epsilon_{12}}{\epsilon_{12}^f}\right)^2 + \left(\frac{\epsilon_{13}}{\epsilon_{13}^f}\right)^2 + \left(\frac{\epsilon_{23}}{\epsilon_{23}^f}\right)^2 \geq 1 & (\epsilon_{22} > 0) \\ \frac{(\epsilon_{22}+\epsilon_{33})^2}{\epsilon_{22}^{f,c}\epsilon_{33}^{f,c}} + \frac{\epsilon_{22}+\epsilon_{33}}{\epsilon_{22}^f} \left( \frac{\epsilon_{22}^{f,c}}{2\epsilon_{12}^f} - 1 \right) - \frac{\epsilon_{22}\epsilon_{33}}{(\epsilon_{23}^f)^2} + \left(\frac{\epsilon_{12}}{\epsilon_{12}^f}\right)^2 \\ \quad + \left(\frac{\epsilon_{13}}{\epsilon_{13}^f}\right)^2 + \left(\frac{\epsilon_{23}}{\epsilon_{23}^f}\right)^2 \geq 1 & (\epsilon_{22} < 0) \end{cases} \quad (4.2)$$

iii) Transverse direction 3,

$$F_z^2 = \begin{cases} \left(\frac{\epsilon_{33}}{\epsilon_{33}^{f,t}}\right)^2 + \left(\frac{\epsilon_{13}}{\epsilon_{13}^f}\right)^2 + \left(\frac{\epsilon_{23}}{\epsilon_{23}^f}\right)^2 \geq 1 & (\epsilon_{33} > 0) \\ \left(\frac{\epsilon_{33}}{\epsilon_{33}^{f,c}}\right)^2 + \left(\frac{\epsilon_{13}}{\epsilon_{13}^f}\right)^2 + \left(\frac{\epsilon_{23}}{\epsilon_{23}^f}\right)^2 \geq 1 & (\epsilon_{33} < 0) \end{cases} \quad (4.3)$$

in which  $\epsilon_{ii}^{f,t} = \frac{\sigma_i^{f,t}}{C_{ii}}$ ,  $\epsilon_{ii}^{f,c} = \frac{\sigma_i^{f,c}}{C_{ii}}$  ( $i = 1, 2, 3$ ),  $\epsilon_{12}^f = \frac{\sigma_{12}^f}{C_{44}}$ ,  $\epsilon_{13}^f = \frac{\sigma_{13}^f}{C_{55}}$ ,  $\epsilon_{23}^f = \frac{\sigma_{23}^f}{C_{66}}$

#### 4.3.4 Modified Hashin's failure criterion

Modified Hashin's failure criterion for plane stress condition is given below

i) Longitudinal direction 1,

$$F_f = \begin{cases} \left[ \left( \frac{\tilde{\sigma}_{11}}{X_T} \right)^2 + \alpha \cdot \left( \frac{\tilde{\sigma}_{12}}{S} \right)^2 \right]^{\frac{1}{2}} \geq 1 & (\tilde{\sigma}_{11} > 0) \\ \left[ \left( \frac{\tilde{\sigma}_{11}}{X_C} \right)^2 + \alpha \cdot \left( \frac{\tilde{\sigma}_{12}}{S} \right)^2 \right]^{\frac{1}{2}} \geq 1 & (\tilde{\sigma}_{11} < 0) \end{cases} \quad (4.4)$$

i) Transverse direction 2,

$$F_f = \begin{cases} \left[ \left( \frac{\tilde{\sigma}_{22}}{Y_T} \right)^2 + \alpha \cdot \left( \frac{\tilde{\sigma}_{12}}{S} \right)^2 \right]^{\frac{1}{2}} \geq 1 & (\tilde{\sigma}_{22} > 0) \\ \left[ \left( \frac{\tilde{\sigma}_{22}}{Y_C} \right)^2 + \alpha \cdot \left( \frac{\tilde{\sigma}_{12}}{S} \right)^2 \right]^{\frac{1}{2}} \geq 1 & (\tilde{\sigma}_{22} < 0) \end{cases} \quad (4.5)$$

where the shear contribution factor  $\alpha$  ranges from 0 to 1.

#### 4.4 Types of damage evolution

Once the damage is initiated in a material point of composite material, the material property must be degraded. This results in strain-softening of the composite materials rather than strain hardening, which is observed in conventional materials like metals. Several post-damage models have been proposed for progressive failure analysis, and most of them belong to one of the following categories: instantaneous unloading, gradual loading, or constant stress at failure material point, as shown in Fig.(4.2)

Since continuum damage mechanics is a more accurate methodology to predict the failure behaviour of composites, non-linear gradual unloading of the composite material is adopted and simulated in this work. Therefore non-linear material properties degradation model is implemented in this work. Based on the type of damage variable chosen, i.e., scalar, vector or second-order tensor, the damage modelling can be classified into isotropic or anisotropic damage modelling. A brief description of the types of damage modelling, damage evolution equation used and material tangent stiffness etc. is given below

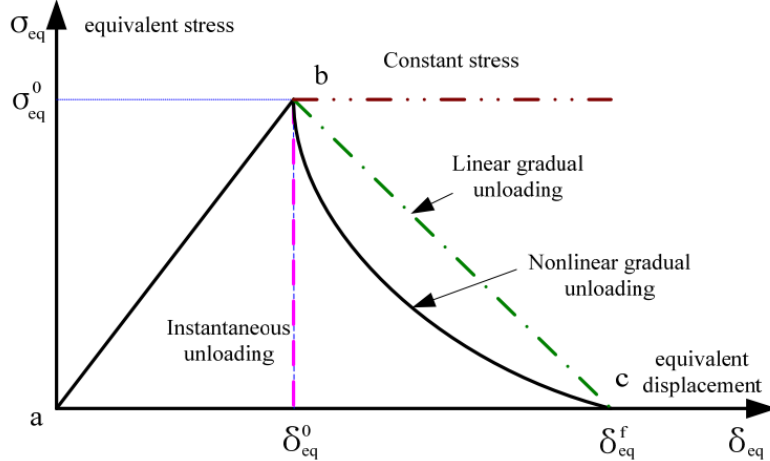


Figure 4.2: Types of degradation behaviour in damaged composite materials

#### 4.4.1 Isotropic damage

In the case of isotropic distribution of cracks, the damage state is usually considered isotropic, and only a scalar variable  $D$  is required to represent the damage state of the material. In this work, a damage evolution law of the following form is considered for calculating damage, once the damage has been initiated

$$D = 1 - e^{-P(\tilde{\epsilon} - k)} \quad (4.6)$$

where  $P$  is the softening parameter which determines the slope of the damage evolution,  $\tilde{\epsilon}$  is 1D equivalent strain and  $k$  is the threshold value. Since the Eqn. (4.6) is an exponential equation, the damage  $D$  evolves exponentially from 0 to 1, and the strain-softening will be an exponential decay function. Once the damage starts to evolve, the material property must be degraded. Therefore the material stiffness matrix of the damaged material is given by,

$$\mathbb{C}(D) = (1 - D)\mathbb{C}_0 \quad (4.7)$$

where  $\mathbb{C}_0$  is the material stiffness matrix of the undamaged material. Therefore the stress-strain relation for a strain softening model is given by,

$$\sigma = \mathbb{C}(D) : \epsilon \quad (4.8)$$

The finite element equations obtained for the strain-softening model are non-linear. Therefore Newton-Raphson technique is used to solve the resulting system of non-linear

equations. To ensure the robustness of the Newton-Raphson method, it is important to compute the material tangent constitutive tensor  $\mathbb{C}_T$ . It can be derived as follows,

$$\begin{aligned}\mathbb{C}_T &= \frac{\partial \sigma}{\partial \epsilon} \\ \sigma &= f(\epsilon, D) \\ \mathbb{C}_T &= \mathbb{C}(D) + \epsilon : \left( \frac{\partial \sigma}{\partial D} \otimes \frac{\partial D}{\partial \epsilon} \right)\end{aligned}\quad (4.9)$$

In the above equation, the first term  $\mathbb{C}(D)$  is the damaged elasticity matrix and second term is due increased damage. In the absence of damage propagation in an increment (For eg., during unloading), the material tangent tensor is equal to the damaged elasticity matrix, so the response is linearly elastic.

#### 4.4.2 Anisotropic damage

In the case of orthotropic materials, the material property changes in the mutually orthogonal direction. Therefore it is more appropriate to choose a second-order damage tensor. In this work, a symmetric second-order tensor  $\underline{D}$  is chosen, whose principal directions are assumed to coincide with the principal material directions. The eigenvalues of the damage tensor  $\underline{D}$  have a simple physical interpretation, i.e., the  $i^{th}$  eigenvalue  $d_i$  represents the effective fractional reduction in load carrying area on planes that are perpendicular to  $i^{th}$  principal material direction. The damage tensor  $\underline{D}$  can be represented as,

$$\underline{D} = \begin{bmatrix} d_1 & 0 & 0 \\ 0 & d_2 & 0 \\ 0 & 0 & d_3 \end{bmatrix}$$

The relationship between damaged and undamaged material must be established so that it helps us derive the constitutive equation (i.e., damaged elastic stiffness matrix) for the damaged material. In this work, the hypothesis of strain energy equivalence (Section 2.8) is used to derive the elastic stiffness matrix of the damaged material. According to the hypothesis of strain energy equivalence, from Eqn. (2.33) the elastic stiffness matrix of the damaged material can be derived as,

$$\mathbb{C}(D) = \mathbb{M}^{-1} : \mathbb{C}_0 : \mathbb{M}^{T,-1} \quad (4.10)$$

where  $\mathbb{M}$  is the damage effect tensor from Section (2.6).

A simple damage evolution law for each principal material direction in case of anisotropic damage is given as follows,

$$d_i = 1 - \frac{e^{-P(F_I-1)}}{F_I} \quad (4.11)$$

where  $d_i$  ( $i = 1,2,3$ ) and  $F_I$  ( $I = f,m,z$ ) are damage evolution and failure index in each principal material direction respectively. The material tangent stiffness tensor for anisotropic damage can also be derived in the same way as isotropic damage and it is given as follows

$$\begin{aligned} \mathbb{C}_T &= \frac{\partial \sigma}{\partial \epsilon} \\ \sigma &= f(\epsilon, \underline{D}) \\ \mathbb{C}_T &= \mathbb{C}(D) + \epsilon : \sum_{i=1}^3 \left( \frac{\partial \sigma}{\partial d_i} \otimes \frac{\partial d_i}{\partial \epsilon} \right) \end{aligned} \quad (4.12)$$

In the above equation, the second term(i.e., due to increased damage) must be computed only if the corresponding failure mode is active. Since the damage evolution equation  $d_i$  depends on failure index, the term  $\frac{\partial d_i}{\partial \epsilon}$  must be computed based on whether the damage happened during tension or compression.

## 4.5 Localisation and Mesh Regularisation

Finite element simulations which use continuum damage models are susceptible to mesh dependency. When the finite element discretization is refined, the numerical problems do not converge to a physically meaningful solution. Because of the strain-softening behaviour of the material, the strain tends to localize, resulting in a strong mesh dependency, i.e., the solution is non-objective with respect to mesh refinement, and the energy dissipated decreases with the decrease in finite element size. Merely improving the numerical solution schemes cannot alleviate the problem associated with mesh dependency and localization. Even if the convergence to the actual solution is improved, the solution may not even make sense from a physical point of view. Therefore the so-called fracture energy regularization is used to reduce the mesh sensitivity. In this technique, the softening law (damage evolution law) is modified so that the amount of energy dissipated over a fully degraded finite element depends on the fracture energy of the material and the finite element size. Therefore the fracture energy( $G_f$ ) of the material and characteristic length ( $L_c$ ) of the finite element must be included in the damage evolution equations. The damage evolution equations based on fracture energy regularization technique for each principal direction is shown below,

In Longitudinal direction 1,

$$d_1 = 1 - \frac{e^{P_1(F_f-1)}}{F_f} \quad (4.13)$$

In transverse direction 2,

$$d_2 = 1 - \frac{e^{P_2(F_m-1)}}{F_m} \quad (4.14)$$

In transverse direction 3,

$$d_3 = 1 - \frac{e^{P_3(F_z-1)}}{F_z} \quad (4.15)$$

where  $P_1 = \frac{-\sigma_{11}^f \epsilon_{11}^f L_c}{G_{f,1}}$ ,  $P_2 = \frac{-\sigma_{22}^f \epsilon_{22}^f L_c}{G_{f,2}}$  and  $P_3 = \frac{-\sigma_{33}^f \epsilon_{33}^f L_c}{G_{f,3}}$

- $G_{f,i}$  - is the fracture energy in each principal direction ( $i = 1,2,3$ )
- $\sigma_{ii}^f$  - failure strength in each principal direction ( $i = 1,2,3$ )
- $\epsilon_{ii}^f$  - failure strain in each principal direction ( $i = 1,2,3$ )

## 4.6 Numerical implementation of the damage model in ANSYS

As discussed before, the material models necessary for simulating progressive damage failure is implemented using the ANSYS user-programmable feature called USERMAT. The damage model implemented using USERMAT computes and updates the current stress and consistent tangent stiffness. The following sections deal with the numerical implementation of the damage model based on two different methods or criteria used to predict the damage initiation.

- Strain based damage model
- Stress based damage model

### 4.6.1 Strain based damage model

In the case of the strain-based damage model, the damage initiation is predicted using current strain ( $\epsilon_{n+1}$ ). The USERMAT receives strains, stresses and state variables at the beginning of the time increment and the current strain increment. The following steps describe the process of implementing the damage model

- Calculate current strain

$$\underline{\epsilon}_{n+1} = \underline{\epsilon}_n + \underline{\Delta\epsilon}$$

- Calculate the current degraded material stiffness matrix  $\mathbb{C}(\underline{D}_n)$
- Calculate the failure indices  $F_I(\underline{\epsilon})$  (Refer Section (4.3.1) and (4.3.3) )

Check if  $F_I \geq F_{I\max}$

- if  $F_I(\underline{\epsilon}) < 1$

$$\underline{\sigma}_{n+1} = \mathbb{C}(\underline{D}_n) : \underline{\epsilon}_{n+1}$$

$$\mathbb{C}_T = \mathbb{C}(\underline{D}_n)$$

- else

Calculate the damage variables using damage evolution law, (Refer Eqn (??) to (??))

$$d_1(F_f), d_2(F_m), d_3(F_z)$$

Check if  $d_i \geq 0$

Calculate the updated degraded stiffness based on damage variables

$$\mathbb{C}(\underline{D}_{n+1})$$

Calculate current stress

$$\underline{\sigma}_{n+1} = \mathbb{C}(\underline{D}_{n+1}) : \underline{\epsilon}_{n+1}$$

Calculate tangent stiffness

$$\mathbb{C}_T = \mathbb{C}(D) + \sum_{i=1}^3 \left( \frac{\partial \mathbb{C}(D)}{\partial d_i} : \epsilon \otimes \frac{\partial d_i}{\partial \epsilon} \right)$$

#### 4.6.2 Stress based damage model

In case of stress-based damage model, the damage initiation is predicted using effective ( $\tilde{\sigma}_{n+1}$ ). The USERMAT receives strains, stresses and state variables at the beginning of the time increment and the current strain increment. The following steps describe the process of implementing the damage model.

- Calculate the elastic stiffness matrix  $\mathbb{C}$
- Calculate effective stress

$$\tilde{\sigma}_{n+1} = \mathbb{C}_0 : \underline{\epsilon}_{n+1}$$

- Calculate the failure indices  $F_I(\underline{\sigma})$ , (Refer Section (4.3.2), (??) and (4.3.4))

Check if  $F_I \geq F_{I\max}$

- if  $F_I(\underline{\sigma}) < 1$

$$\underline{\sigma}_{n+1} = \tilde{\underline{\sigma}}_{n+1}$$

$$\mathbb{C}_T = \mathbb{C}$$

- else

Calculate the damage variables using damage evolution law, (Refer Eqn (??) to (??))

$$d_1(F_f), d_2(F_m), d_3(F_z)$$

Check if  $d_i \geq 0$

Calculate the updated degraded stiffness based on damage variables

$$\mathbb{C}(D_{n+1})$$

Calculate current stress

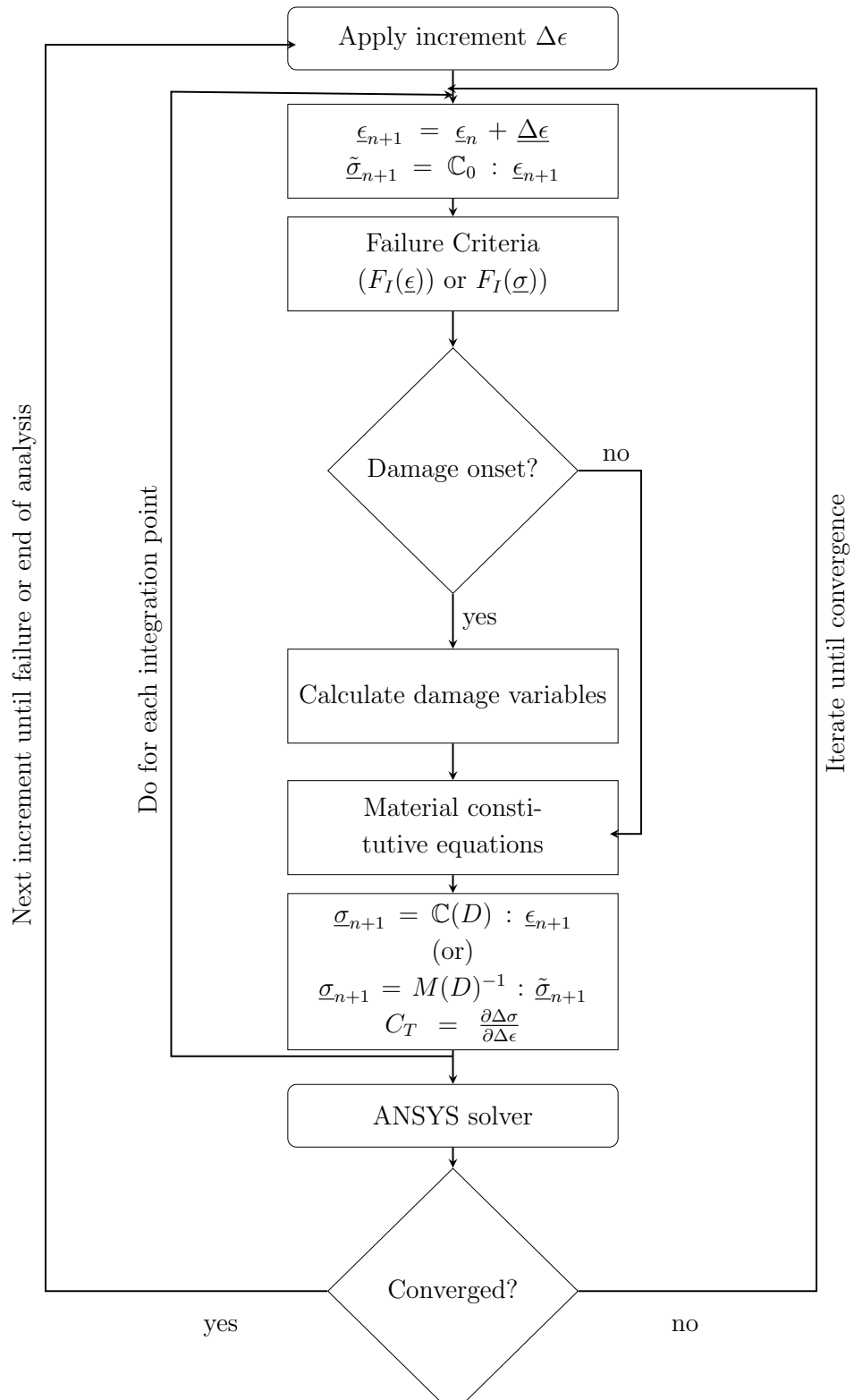
$$\underline{\sigma}_{n+1} = M(D)^{-1} : \tilde{\underline{\sigma}}_{n+1}$$

Calculate tangent stiffness

$$\mathbb{C}_T = \mathbb{C}(D) + \sum_{i=1}^3 \left( \frac{\partial \mathbb{C}(D)}{\partial d_i} : \epsilon \otimes \frac{\partial d_i}{\partial \epsilon} \right)$$

## 4.7 Schematic of UMAT implementation

The flowchart below shows the schematic of the user material subroutine (USER-MAT) implementation for both and strain and stress based damage model and how the subroutine interacts with the ANSYS environment.





# Chapter 5

## Results and Discussion

### 5.1 Modelling Linear elastic behaviour of orthotropic materials

Before implementing the damage behaviour in orthotropic materials, their linear elastic behaviour must be implemented which demonstrates what happens before the damage initiation. As mentioned before orthotropic materials are a special class of material whose properties change in mutually perpendicular directions. Therefore 9 independent material constants are required to model their elastic behaviour numerically. Table (5.1) summarises the utilised material parameters. The constitutive matrix given in the section (2.9) and Hooke's law helps us model the elastic behaviour of the orthotropic materials.

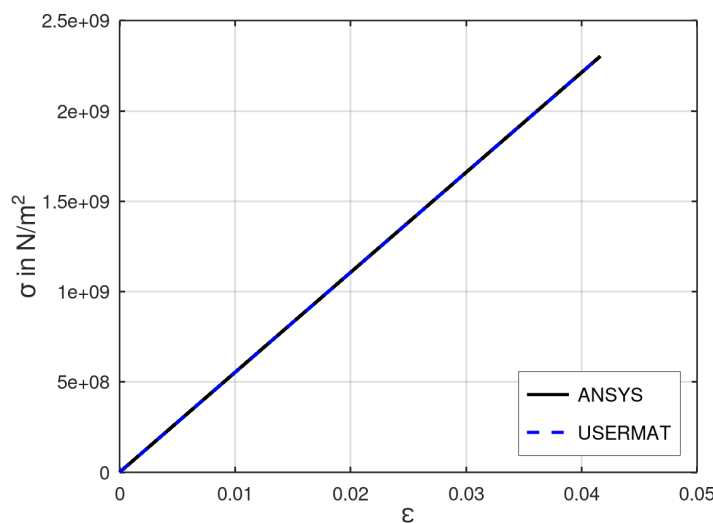
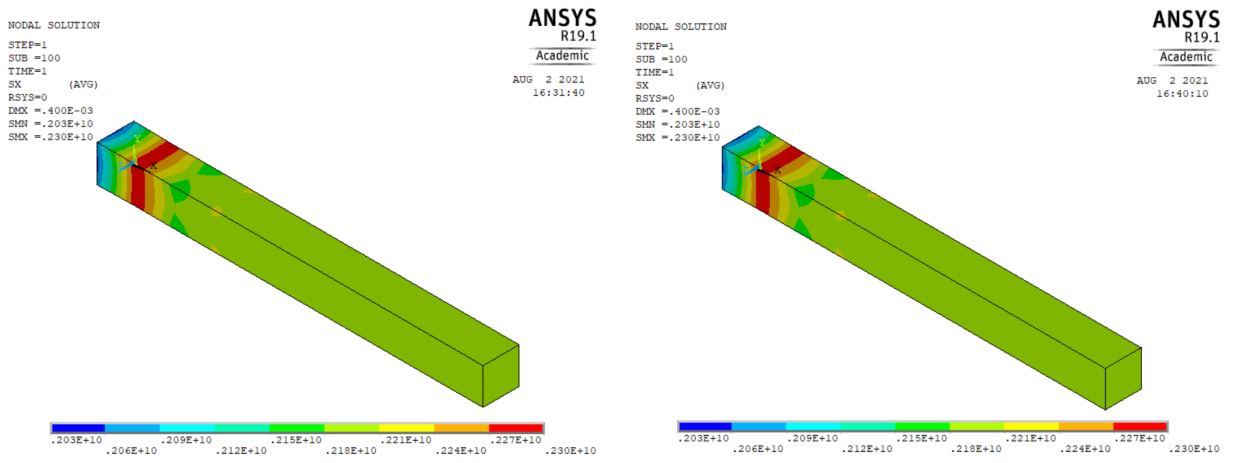


Figure 5.1: Stress-Strain relation (ANSYS vs USERMAT)

Symbol	Material Parameter	Value
$E_1$	Longitudinal (fibre dominated) elastic modulus	55000e6 N/m <sup>2</sup>
$E_2 = E_3$	Transverse(matrix dominated) elastic modulus	9500e6 N/m <sup>2</sup>
$\nu_{12} = \nu_{13}$	Poisson's ratio (in-plane)	0.33
$\nu_{23}$	Poisson's ratio (Planes 2-3)	0.27
$G_{12} = G_{13}$	In-plane shear modulus	5500e6 N/m <sup>2</sup>
$G_{23}$	Shear modulus (Planes 2-3)	3000e6 N/m <sup>2</sup>
$X_t$	Longitudinal (fibre dominated) Tensile strength	2500e6 N/m <sup>2</sup>
$X_c$	Longitudinal (fibre dominated) Compressive strength	-2000e6 N/m <sup>2</sup>
$Y_t$	Transverse (matrix dominated) Tensile strength	50e6 N/m <sup>2</sup>
$Y_c$	Transverse (matrix dominated) Compressive strength	-200e6 N/m <sup>2</sup>
$S_{12}$	In-plane strength	50e6 N/m <sup>2</sup>

Table 5.1: Material parameters(Integration point studies)

The linear elastic behaviour of the orthotropic material is implemented in the USERMAT using constitutive equations, and in this section, the results obtained are compared against the default orthotropic material option present in ANSYS using a structural example. A bar of length 10mm and area 1mm<sup>2</sup> ( $b = 1\text{mm}$ ,  $t = 1\text{mm}$ ) fixed at one end is chosen for the analysis. The bar is constructed using 8 node SOLID 185 elements, and full integration has been used. A displacement of 1mm is applied at the free end, and the results obtained using the ANSYS default and the USERMAT are presented below. The figure (5.1) compares the stress-strain relation of the bar obtained using both ANSYS default and USERMAT



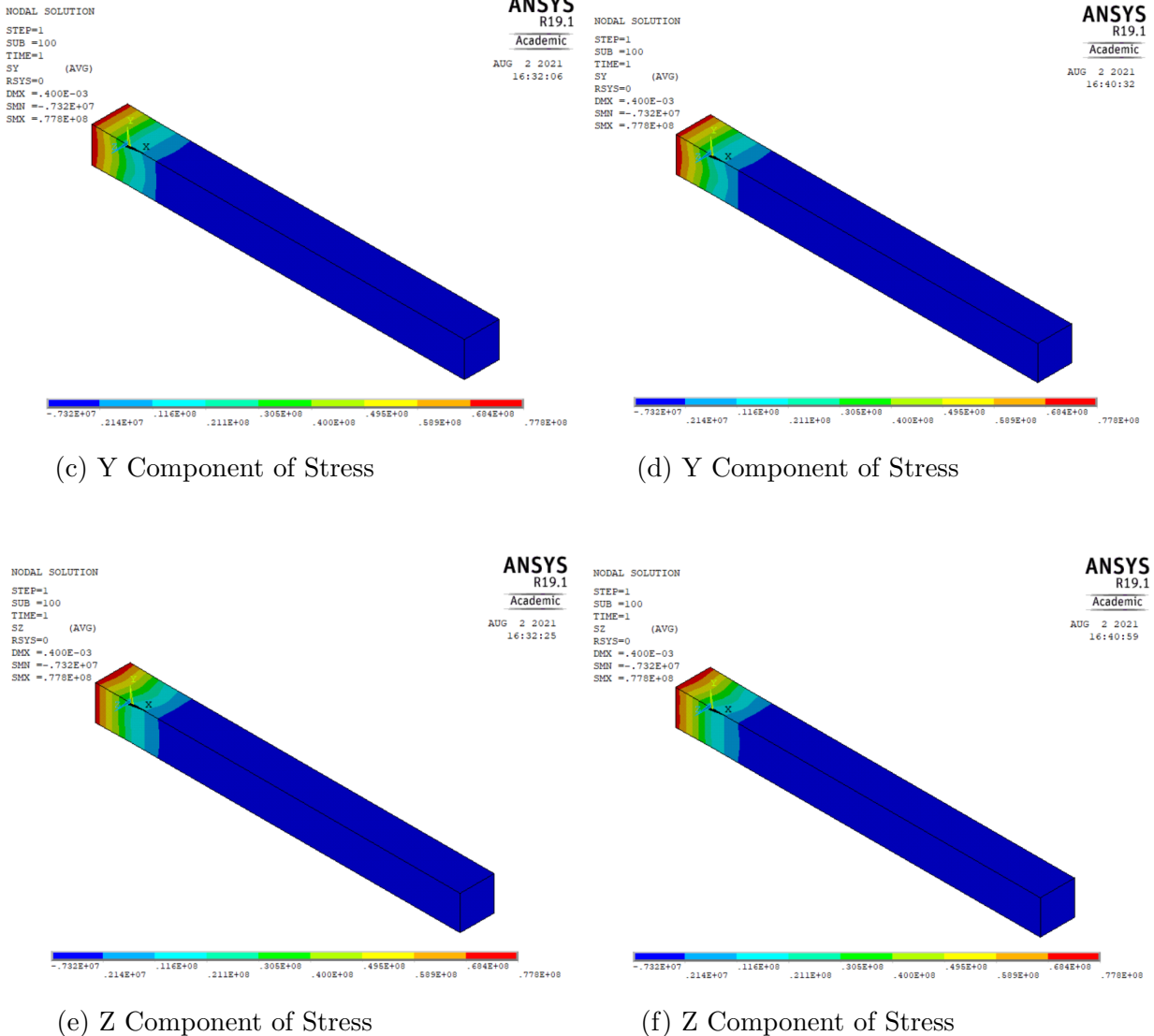


Figure 5.2: Contour plots of the stress components  $\sigma_{xx}$ ,  $\sigma_{yy}$  and  $\sigma_{zz}$  of the bar obtained using ANSYS(Figures a,c,e on the left) and USERMAT(Figures b,d,f on the right)

Figure (5.2) shows the contour plots of the normal stresses ( $\sigma_{xx}$ ,  $\sigma_{yy}$  and  $\sigma_{zz}$ ) computed using ANSYS default and USERMAT respectively. The comparison of the stress-strain relation and contour plots between the ANSYS default and USERMAT confirms that the results obtained using both options are same and therefore further damage-initiation and damage-evolution processes can now be implemented.

## 5.2 Damage behaviour at integration point level

The material subroutines are first developed on the octave and tested using constitutive driver routines, enabling us to understand the phenomenon at the integration point level. In order to demonstrate the evolution of damage after damage initiation and the strain-softening, following simple loading cases are investigated at the integration point level.

- Uniaxial tension
- Biaxial tension
- Triaxial tension.

After that, the material subroutines are implemented in USERMAT and tested in the ANSYS environment using a 3D finite element of unit length. The finite element is subjected to the above loading cases, and the results are compared against the octave implementation

### 5.2.1 Uniaxial tension

In the case of uniaxial tension, the normal stress is present only in one direction, and the shear stresses are zero, i.e., only one component (diagonal) of the stress tensor is non-zero. In the Ansys environment, uniaxial tension is achieved by applying a displacement on the finite element in a normal direction (11), which increases the strain  $\epsilon_{11}$  linearly, and the lateral (transverse) contraction is not constrained. 3D Hashin's quadratic strain criteria (Section(4.3.3)) is used to predict the damage initiation, and exponential damage evolution law (Eqn(4.11)) is used to calculate the damage evolution. The results obtained from Ansys and usermat are presented in the Figure (5.3a) and (5.3b) respectively. The Figure (5.4) shows the evolution of damage variables. The system is linearly elastic till the damage initiation strain, and the damage is zero. Once the strain  $\epsilon_{11}$  exceeds the damage initiation strain, the damage  $d_1$  starts to evolve exponentially, and the stress starts to drop due to the reduction in stiffness in 11 direction. The damage variables  $d_2$  and  $d_3$  are zero. The comparison between the figures (5.3a) and (5.3b) suggests that the material routine implemented in Octave and usermat are numerically similar to each other.

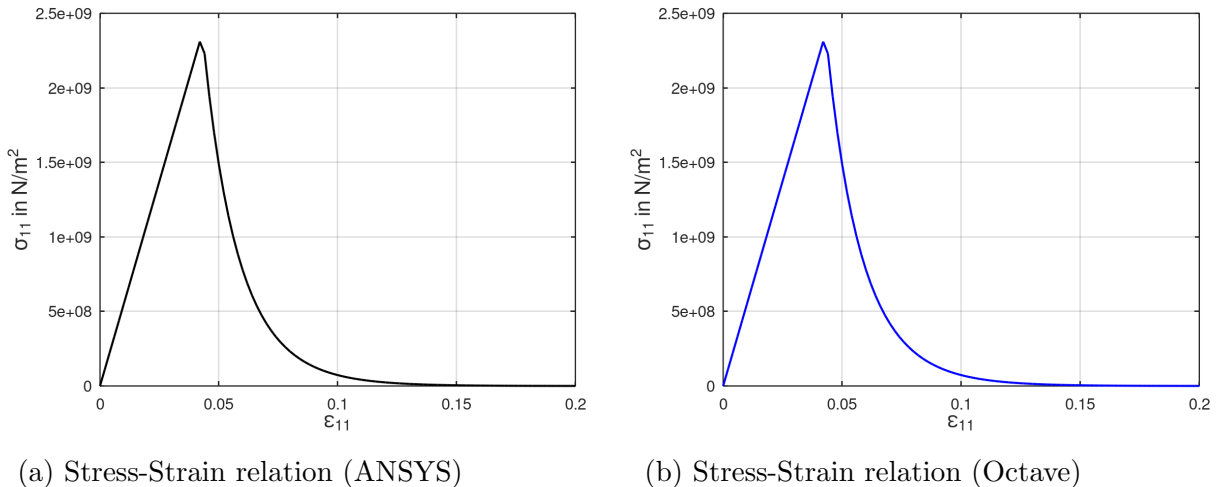


Figure 5.3: Evolution of stress for uniaxial tension test in 11 direction

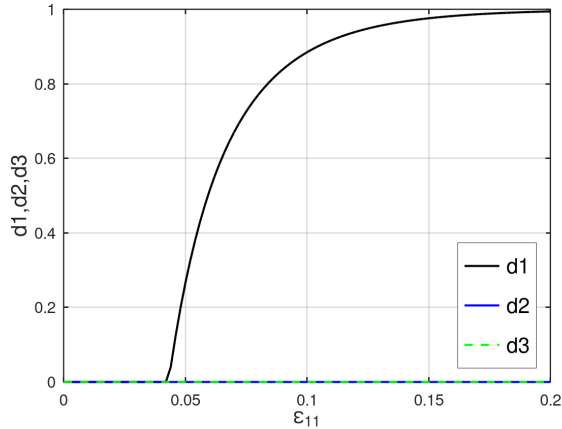


Figure 5.4: Evolution of damage components for uniaxial tension test in 11 direction

The scalar softening parameter( $P$ ) in the damage evolution equation(4.11) determines the slope of the damage curve. The following figure demonstrates the influence of the softening parameter ( $P$ ) in the damage evolution

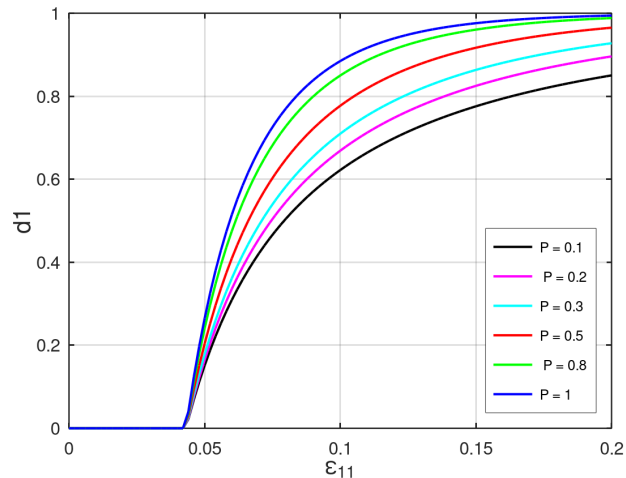


Figure 5.5: Influence of softening parameter  $P$  in the damage evolution)

### Drawbacks of strain based damage initiation criteria

Since the lateral contraction is not constrained during uniaxial tension, the transverse directions experience compression due to Poisson's effect, i.e.,  $\epsilon_{22}$  and  $\epsilon_{33}$  will be negative. If the compressive strength in the transverse directions 2 and 3 are sufficiently low, the strains  $\epsilon_{22}$  and  $\epsilon_{33}$  will exceed the damage initiation strain. This leads to damage evolution without the presence of stress in transverse directions 2 and 3. This phenomenon cause convergence issues and the model stops when the damage evolves without the presence of stress. The image (5.6) shows the norm of the residual

stress, which does not reach zero (or a tolerance) after 100 iterations of the Newton-raphson, which indicates the failure of the model to converge to a solution when using low compressive strength in the transverse direction ( $Y_c = -180\text{MPa}$ )

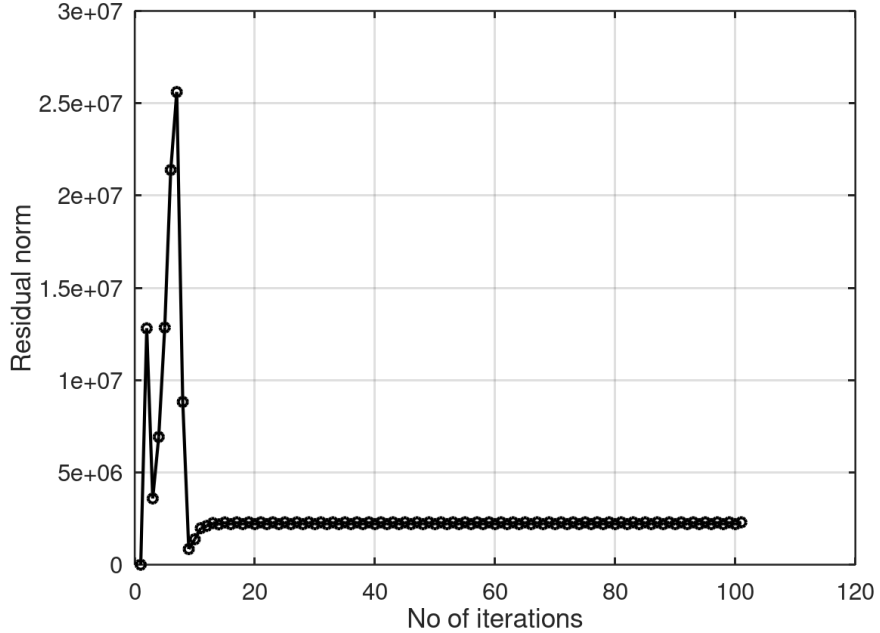


Figure 5.6: Convergence issue: Residual norm of the stress *vs* No of Newton-raphson iterations

This problem can be rectified by using stress-based damage initiation criteria. Since damage evolution depends on failure index  $F$ , the transverse failure indices  $F_m$  and  $F_z$  will be zero during uniaxial tension if the stress-based damage initiation criteria are used. This results in zero damage in the transverse direction. The following section presents the results obtained using stress-based damage initiation and the use of mesh regularisation in the damage evolution law.

### Stress based damage initiation and mesh regularisation

As mentioned in the section (4.5), the strain localisation problems result in strong mesh dependency, so fracture energy, and characteristic length( $L_c$ ) of the element has to been included in the damage evolution law in order to alleviate the problem. So the material routine is modified by changing the damage initiation criteria to maximum stress criteria(4.2) and including the damage evolution equations from (4.13) to (4.15). The uniaxial tension is conducted again with the changes mentioned above and with very low transverse compression strength, and the results are presented below

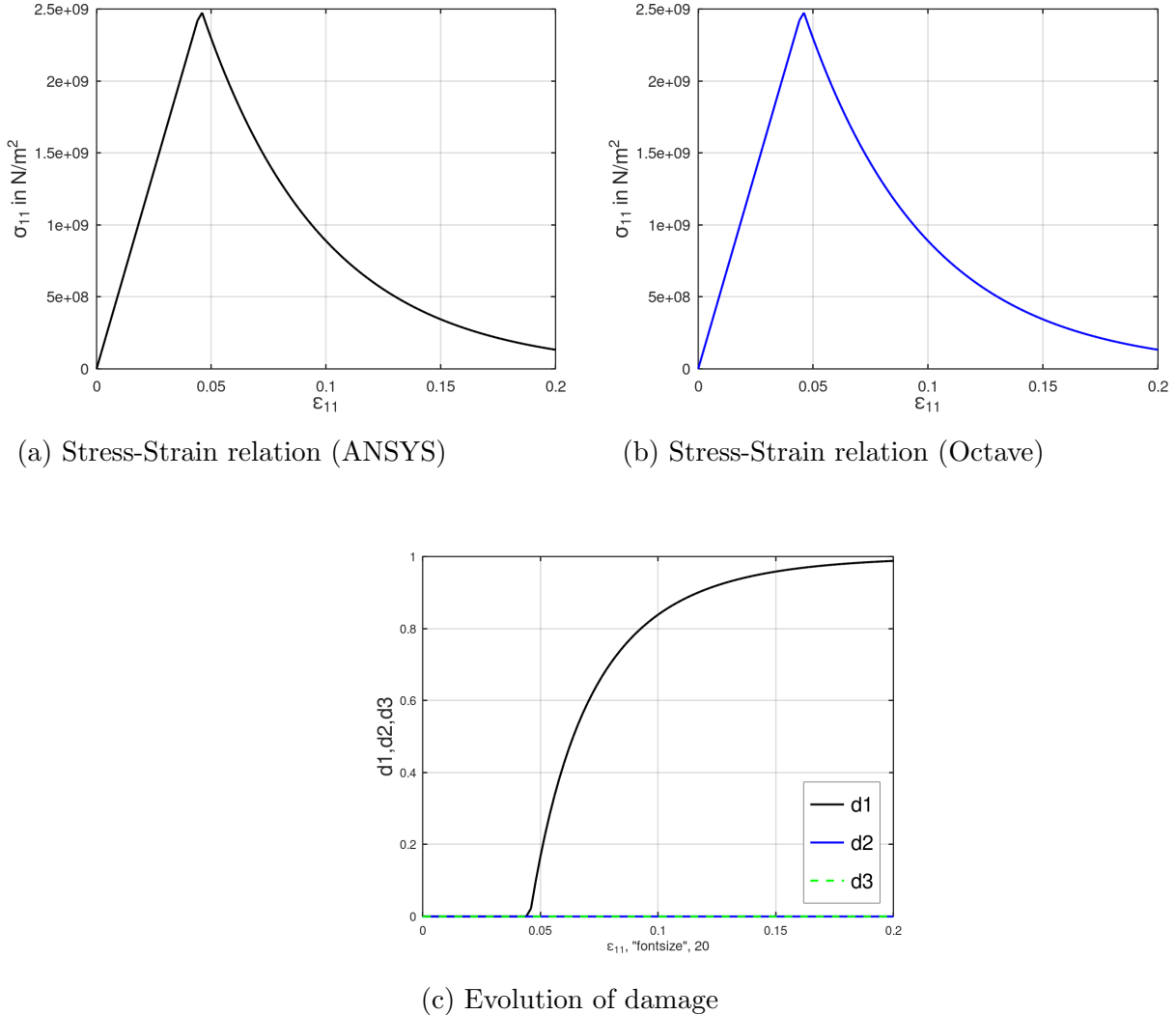


Figure 5.7: Evolution of stress and damage components with stress-based damage initiation criteria under uniaxial tension

From figure (5.7c) it is evident that the damage  $d_2$  and  $d_3$  are zero as a result of stress-based damage initiation because the stress components  $\sigma_{22}$  and  $\sigma_{33}$  are zero under uniaxial tension. While using mesh regularisation, the slope of the damage curve is determined by the characteristic length ( $L_c$ ), which depends on the volume of the element. The following figure (5.5) shows how the damage evolution is affected by the volume of the element,

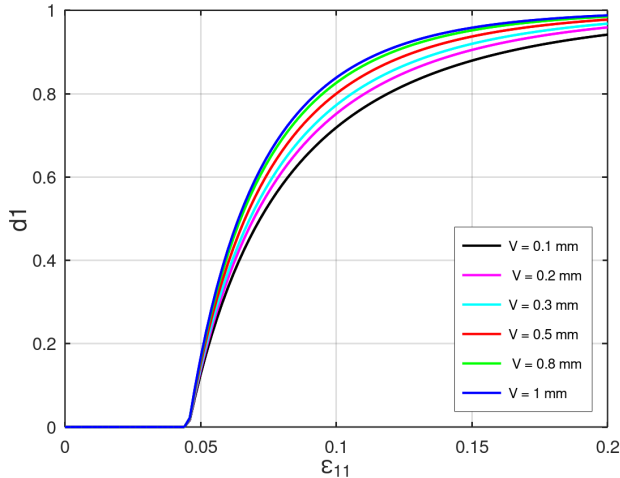


Figure 5.8: Influence of element volume ( $V$ ) in the damage evolution

### Discussion about tangent stiffness

In the case of uniaxial tension, the components of the stress tensor other than  $\sigma_{11}$  are zero. Since stress conditions are enforced, the octave driver routine uses the Newton-raphson method to determine the input strain components other than  $\epsilon_{11}$  iteratively. The Newton-raphson method requires tangent stiffness for computation which can be derived using the equation (4.12) for anisotropic damage. This enables us to test the derived algorithmic tangent stiffness (ATS) before implementing it in USERMAT, which Ansys then uses to solve the non-linear system of equations that arise due to strain softening. The derived algorithmic tangent stiffness is verified by comparing it with the numerical tangent stiffness computed using numerical perturbation. In numerical perturbation, the coefficients of strain tensor are perturbed by a very small value i.e.,  $\Delta\epsilon_{kl}^{n+1} = \delta$  (where  $\delta \ll 1$ ) and the resulting stress perturbations are calculated.

$$\Delta\sigma_{ij}^{n+1} = \sigma_{ij}^{n+1}(\epsilon_{kl}^{n+1} + \delta) - \sigma_{ij}^{n+1}(\epsilon_{kl}^{n+1}) \quad (5.1)$$

Then the components of the tangent stiffness tensor can be estimated as

$$C_T = \frac{\Delta\sigma_{ij}^{n+1}}{\Delta\epsilon_{kl}^{n+1}} \quad (5.2)$$

Since the material routine must be evaluated for every perturbation of  $\epsilon_{kl}$  the routine has to be called six time recursively per load-step iteration. The figure (5.9a) and (5.9b) shows the strain components  $\epsilon_{22}$  and  $\epsilon_{33}$  computed using algorithmic and numerical tangent stiffness which are plotted against  $\epsilon_{11}$  respectively.

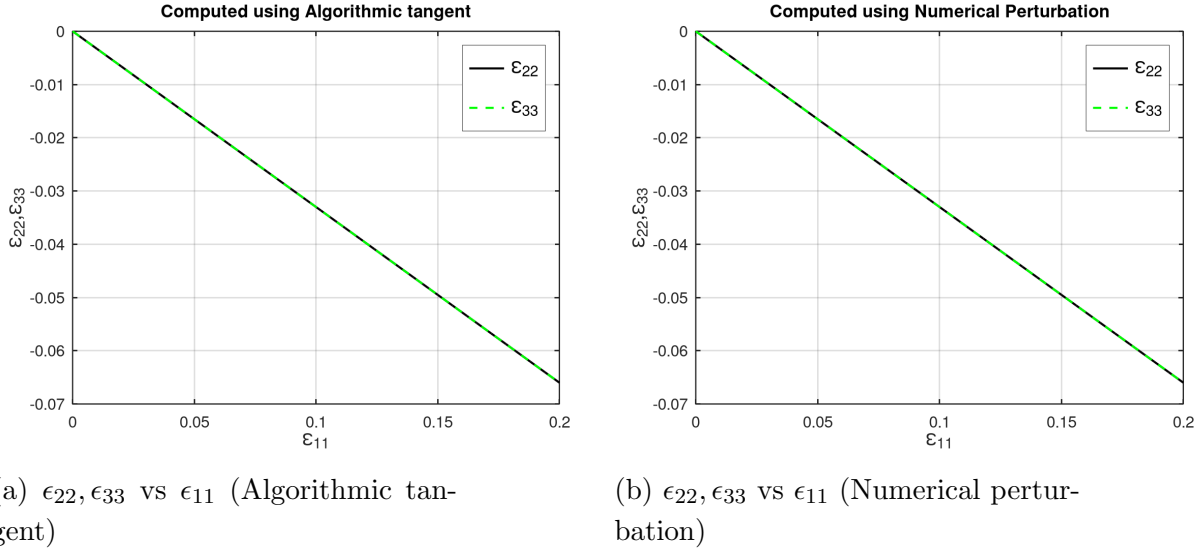
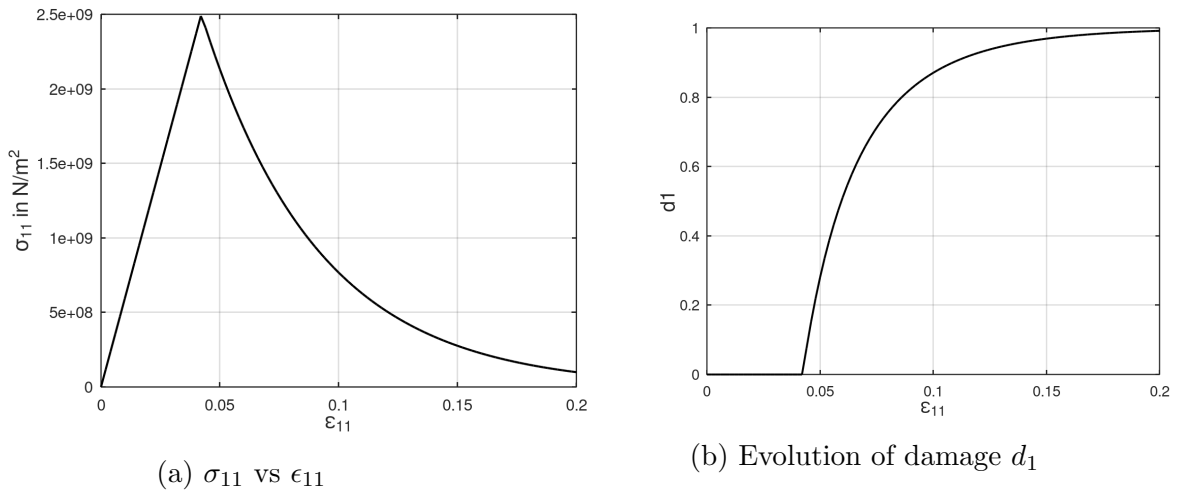


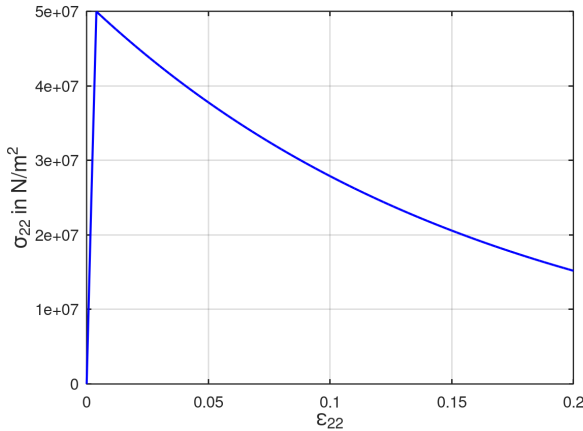
Figure 5.9: The Strain components  $\epsilon_{22}$  and  $\epsilon_{33}$  computed using algorithmic(a) and numerical tangent stiffness(b) under uniaxial tension

These comparison between above plots clearly indicates that the tangent stiffness computed using algorithmic tangent and numerical tangent are numerically similar to each other.

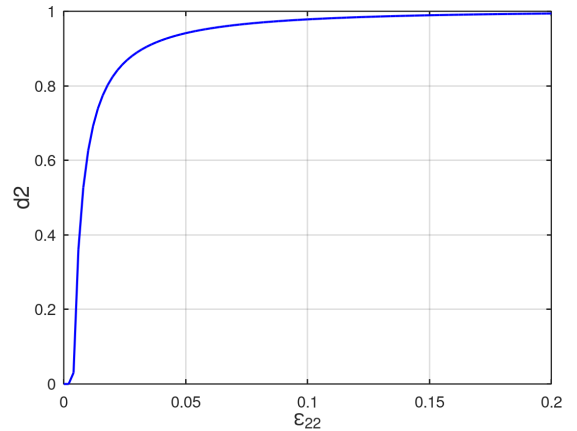
### 5.2.2 Biaxial tension

In the case of biaxial tension, normal stresses are present only in two normal directions, and all the shear stresses are zero i.e., only two components(diagonal) of the stress tensor are non-zero. In Ansys, biaxial tension is achieved by applying the same displacements in two normal directions of the finite element (11 and 22 direction), and the contraction in the third direction (33) is unconstrained. The following figures show the corresponding stress and damage components obtained from the test.





(c)  $\sigma_{22}$  vs  $\epsilon_{22}$



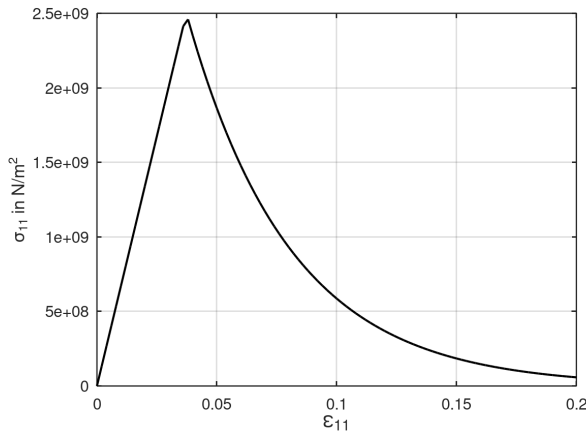
(d) Evolution of damage  $d_2$

Figure 5.10: Evolution of stress(Figures a,c on the left) and corresponding damage(FIGURE b,d on the right) components under biaxial tension

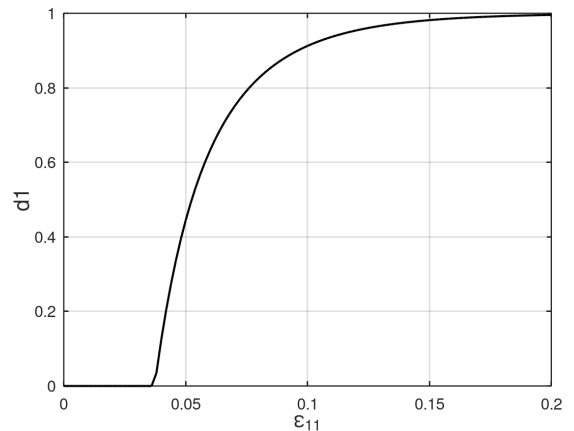
Since the tensile strength in transverse direction is very low compared to the longitudinal direction, evolution of damage ( $d_2$ ) begins very soon and simultaneously the stress component ( $\sigma_{22}$ ) drops as seen in figures (5.10c) and (5.10d).

### 5.2.3 Triaxial tension

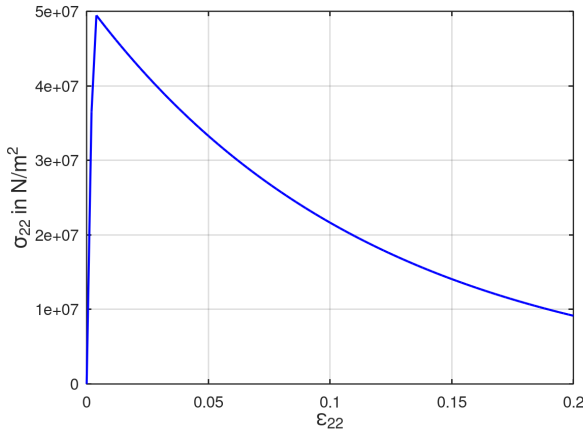
In the case of triaxial tension, the normal stresses are present in all three normal directions, and all the shear stresses are zero, i.e., only diagonal components of the stress tensor are non-zero. In Ansys, triaxial tension is achieved by applying the same displacement in all three normal directions (11, 22 and 33 direction). The following figures show the corresponding stress and damage components obtained from the test.



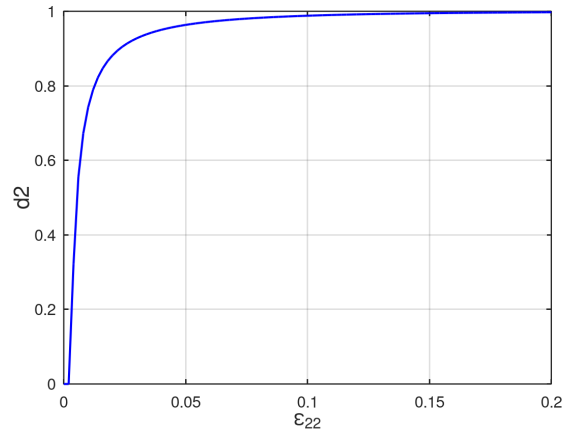
(a)  $\sigma_{11}$  vs  $\epsilon_{11}$



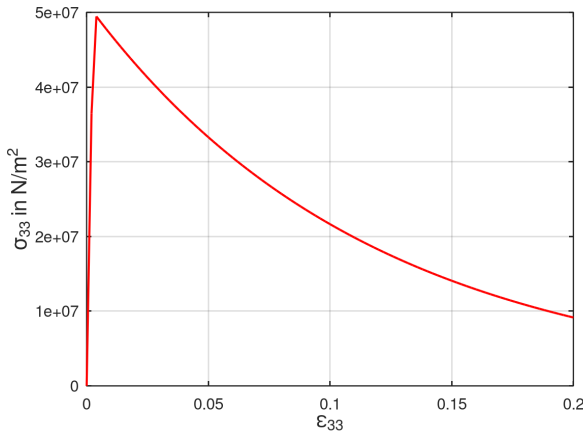
(b) Evolution of damage  $d_1$



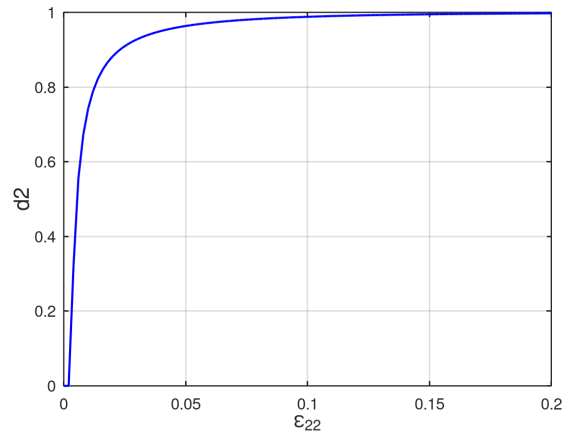
(c)  $\sigma_{22}$  vs  $\epsilon_{22}$



(d) Evolution of damage  $d_2$



(e)  $\sigma_{33}$  vs  $\epsilon_{33}$



(f) Evolution of damage  $d_3$

Figure 5.11: Evolution of stress(Figures a,c,e on the left) and corresponding(Figures b,d,f on the right) damage components under triaxial tension

Since the material properties are same in 22 and 33 direction and the tensile strength is very low compared to the longitudinal direction, the damage  $d_2$  and  $d_3$  evolves simultaneously (Fig (5.11d) and (5.11f)) and very soon as expected. Therefore the stress components  $\sigma_{22}$  and  $\sigma_{33}$  drops very soon as shown in the figure (5.11c) and (5.11e)

### 5.3 Representative structural examples

The following structural examples are used to test the damage model developed in UMAT in the ANSYS environment

- Notched tensile specimen (2D-Plane stress)
- Compact tension(CT) specimen (2D-Plane stress)

- Plate with hole (3D)

Each model is chosen to represent specific features of the damage model. These features include, at first, the capability of the model to represent damage initiation and propagation and secondly, the calculation of multiple damage variables, i.e., the ability to show anisotropic damage development in the composite material when a load is applied(damage plots of multiple damage variable) in both 2D and 3D. Furthermore, mesh convergence studies are done to show that the regularization scheme used gives better results than the non-regularized model. For all the finite element simulations of the above models, linear quadrilateral elements are used (both 2D and 3D) with full Gauss integration. The line search option has been enabled during all simulations in order to get good convergence. The material parameters used for the finite element simulations are given in the Table (5.2)

Symbol	Material Parameter	Value
$E_1$	Longitudinal (fibre dominated) elastic modulus	55.8 GPa
$E_2 = E_3$	Transverse(matrix dominated) elastic modulus	54.9 GPa
$\nu_{12}$	Poisson's ratio	0.043
$G_{12}$	Shear modulus	4.2 GPa
$X_t$	Longitudinal (fibre dominated) Tensile strength	910.1 MPa
$X_c$	Longitudinal (fibre dominated) Compressive strength	-710.2 MPa
$Y_t$	Transverse (matrix dominated) Tensile strength	772.2 MPa
$Y_c$	Transverse (matrix dominated) Compressive strength	-703.3 MPa
$S_{12}$	In-plane strength	131 MPa
$G_f^{ft}$	Tensile fracture energy along Longitudinal direction	125 KJ/m <sup>2</sup>
$G_f^{fc}$	Compressive fracture energy along Longitudinal direction	250 KJ/m <sup>2</sup>
$G_f^{mt}$	Tensile fracture energy along Transverse direction	95 KJ/m <sup>2</sup>
$G_f^{mc}$	Compressive fracture energy along Transverse direction	254 KJ/m <sup>2</sup>

Table 5.2: Material parameters (Representative structural examples)

### 5.3.1 Notched tensile specimen

The first example will demonstrate the model's capability to represent damage initiation and propagation. Because of the symmetry, only one-quarter of the specimen is modelled in the finite element analysis. The appropriate symmetry boundary conditions have been applied at the axis of the symmetry, and the geometry and boundary

conditions are shown in the Figure (5.12). The meshes consist of plane-stress elements (PLANE 182) with bilinear interpolations for displacements, and 2\*2 Gauss integration has been utilized. Three different finite element meshes have been used in the fracture zone with the elements of  $h=1\text{mm}$ ,  $0.5\text{mm}$ ,  $0.25\text{mm}$  and a total of 500, 840, 1460 elements respectively for the convergence studies (Figure 5.13). At first, the longitudinal direction is kept parallel to the loading direction, and the behaviour of the model is analyzed by applying displacement controlled load ( $U_x$ ) in the longitudinal direction (X-direction). The strength in the longitudinal direction is mostly determined by the presence of fibres that have more tensile strength compared to the polymer matrix. Maximum stress criterion (Section 4.3.2) has been used to predict the damage initiation.

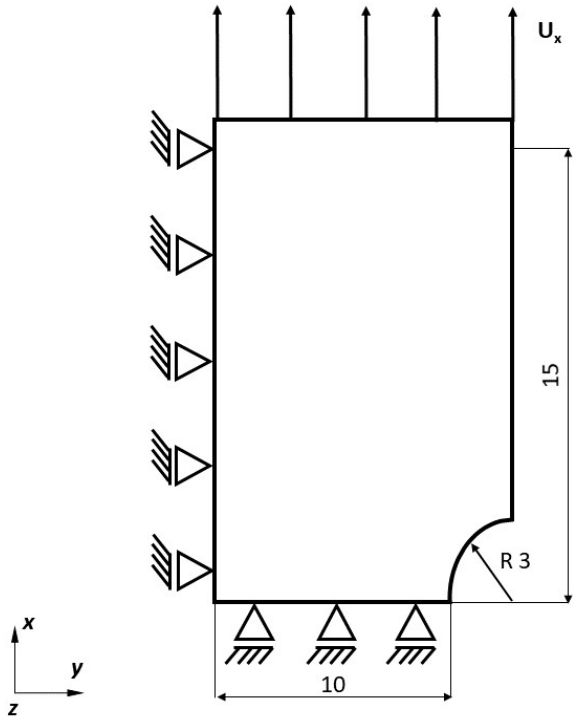


Figure 5.12: Specimen geometry and boundary conditions. Dimensions are given in mm. Displacement controlled loading  $U_x$  is applied

The force-displacement response for the three different meshes with and without the regularization (Section(4.5)) schemes have been plotted in the Figure (5.14a) and (5.14b) respectively. The global-force displacement response is characterized by a large linear regime followed by a gradual drop of load (because of the softening) or a sudden drop in case of no regularization. From figure (5.14), it is clearly evident that the model with regularization gives a stable force-displacement response compared to the model without regularization, where the maximum load capacity is very low, and the load drops significantly with the decrease in mesh size (or increase in the number of elements). Even though the regularization scheme does not

fully alleviate the mesh dependency, it improves the solution significantly compared to the material model without regularization.

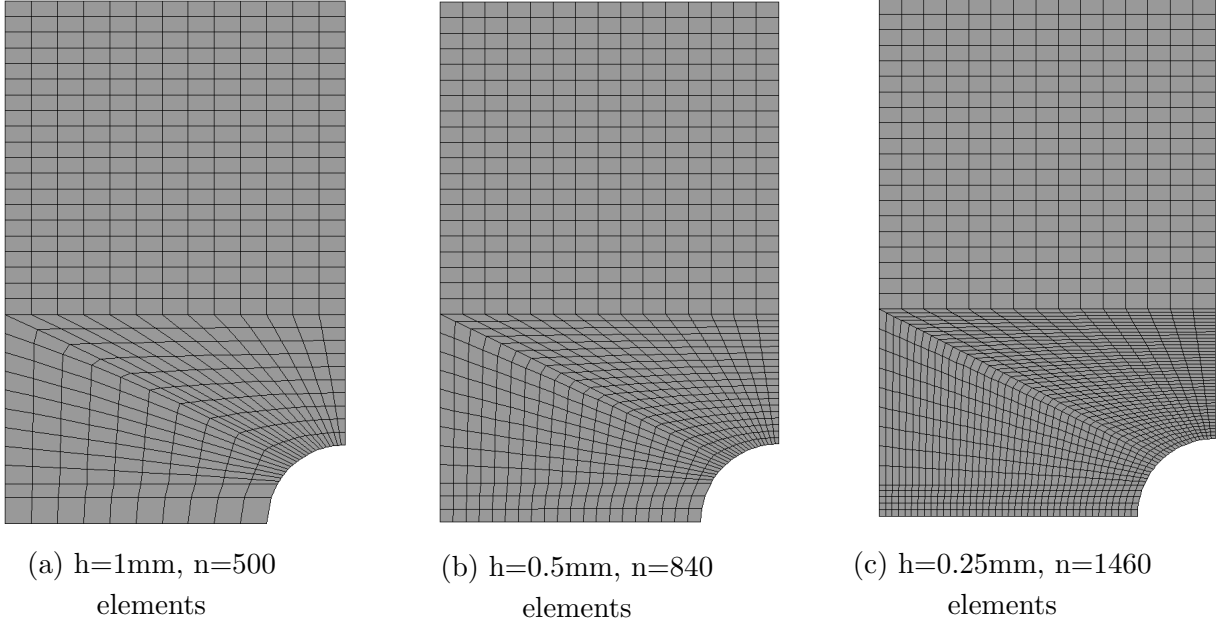


Figure 5.13: Considered meshes ( $h$  is the length of the element along fracture zone and  $n$  the total number of elements)

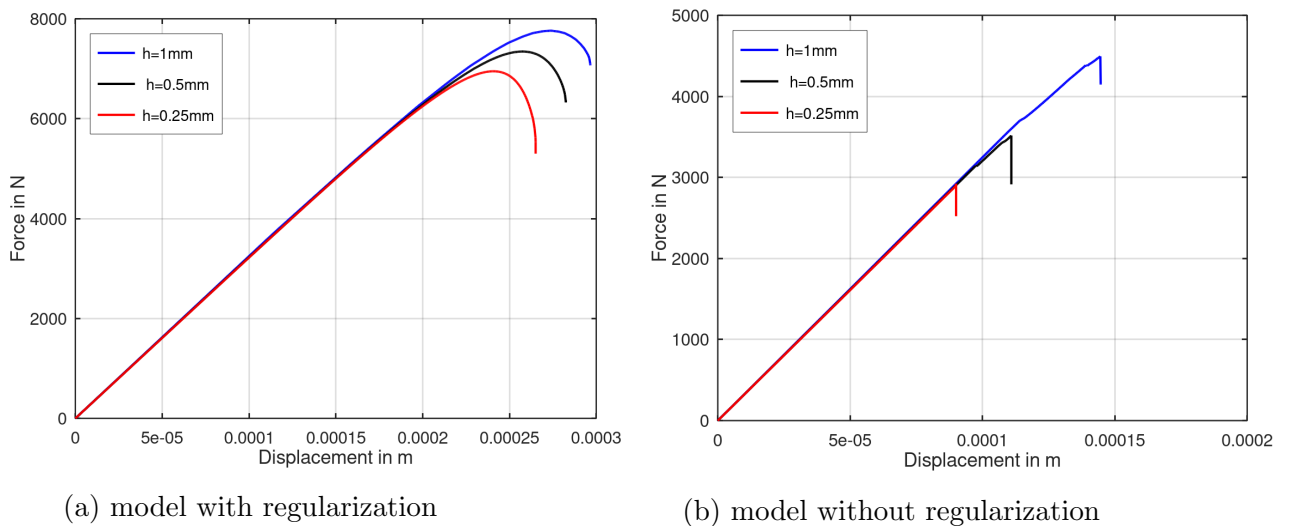
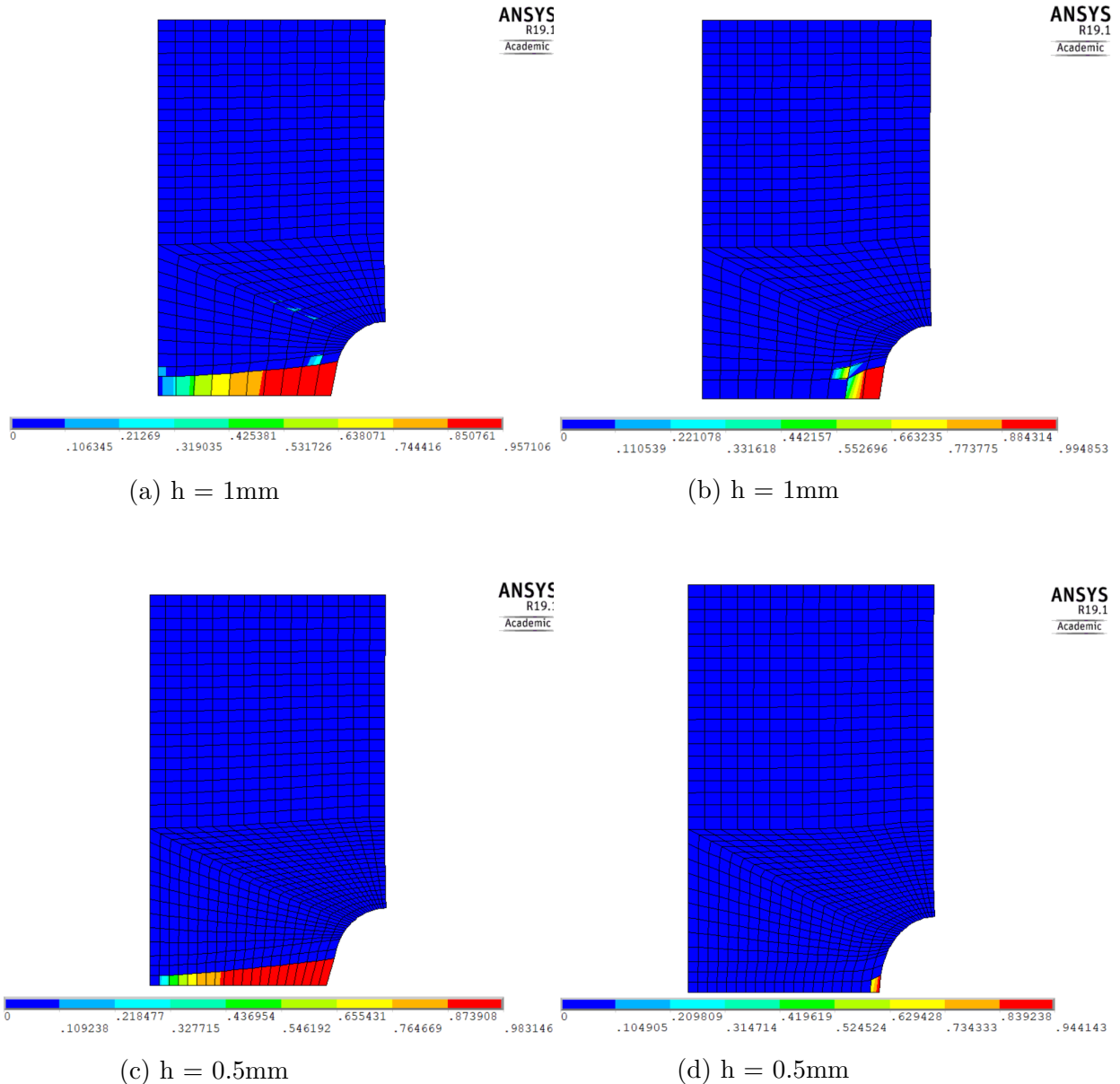


Figure 5.14: Convergence study: Global force-displacement response for model with regularization(Figures a,c,e on the left) and without regularization(Figures b,d,f on the right)

The damage distributions at the end of the process have been plotted for the three different meshes in the Figure (5.15). For numerical reasons the maximum damage is limited to a value of  $d_{max} = 0.9999$ . The improvement in the global response

by using regularization schemes has been illustrated by the damage distributions at the end of the loading process. A relatively large portion of the fracture zone takes part in the damage process instead of very few elements (one or two elements) in the case of no regularization. Damage initiates at the tip of the blunt notch and propagates perpendicular to the loading direction. The width of the damage zone is approximately the same in the three discretizations, but the number of elements that reach a critical damage value (red) increases with the increase in the number of elements along the fracture zone.



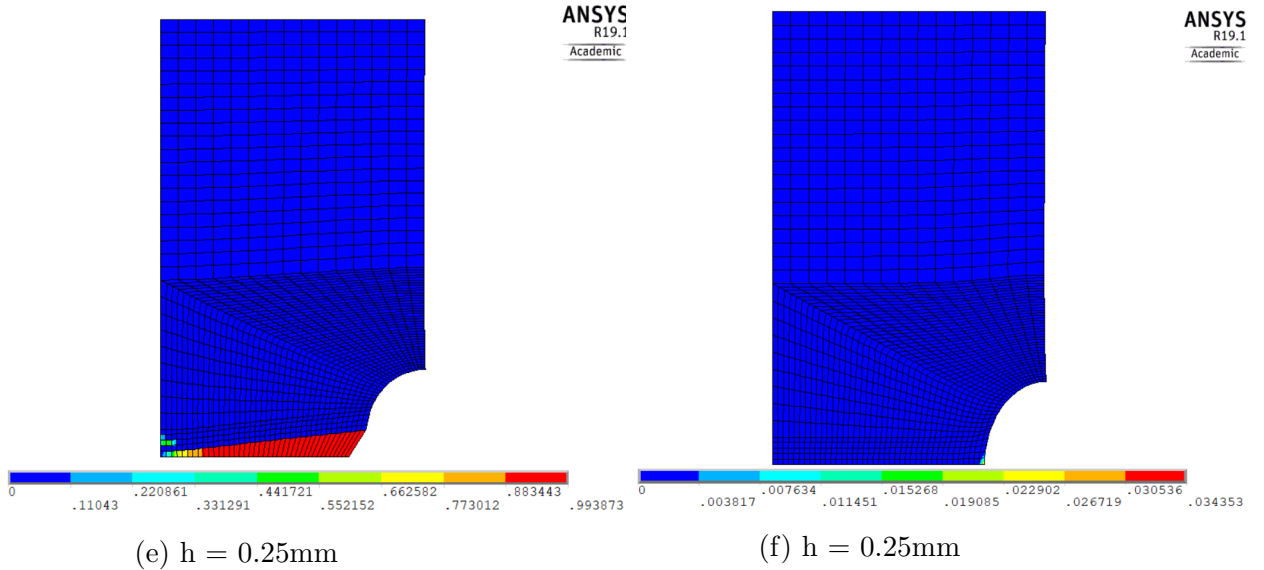
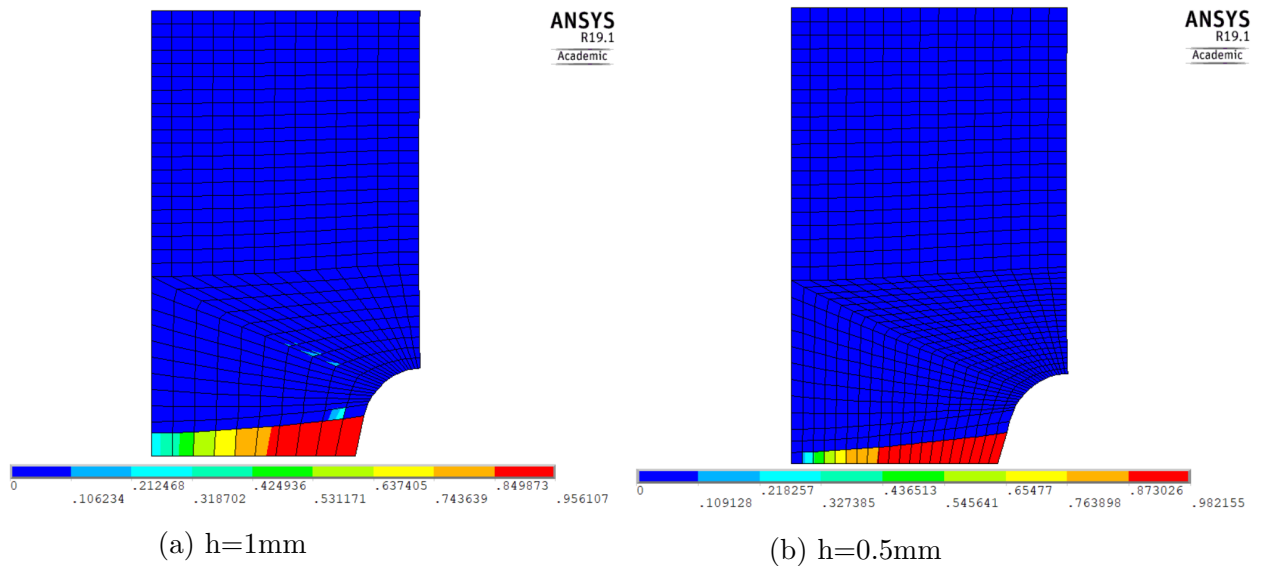
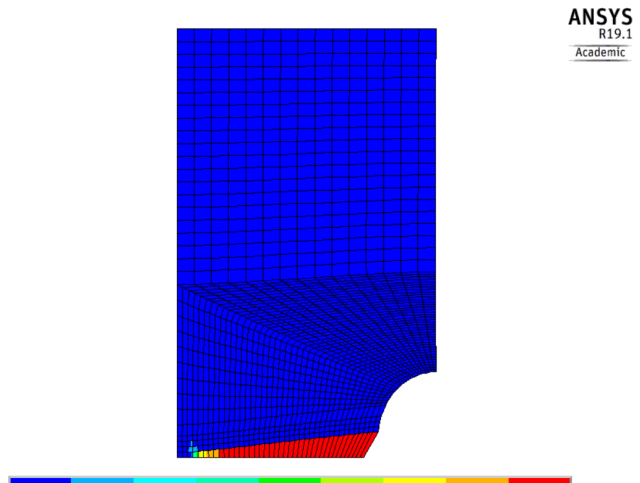


Figure 5.15: Convergence study for model with(Figure a,c,e) and without(b,d,f) regularization: Damage contour plots  $d_1$  at the end of the loading

Now the transverse direction is kept parallel to the loading direction, and the behaviour of the damage model, i.e., initiation and propagation of damage  $d_2$ , is analysed by applying a tensile load in the transverse direction. The strength in the transverse direction is mostly determined by the presence of the polymer matrix, which has less tensile strength than the fibres in the longitudinal direction. The damage ( $d_2$ ) at the end of the loading process is shown in the Figure (5.16)





(c)  $h=0.25\text{mm}$

Figure 5.16: Damage contour plots  $d_2$  at the end of the loading (Loading in transverse direction)

The damage pattern looks similar to the damage ( $d_1$ ) when loaded in the longitudinal direction, i.e., a large portion of the fracture zone got damaged, and the no of elements reaching critical damage increase with the increase in no of elements. The force-displacement response of both longitudinal and transverse loading for a single mesh type ( $h = 0.5\text{mm}$ ) is compared in the Figure (5.17). As expected, the strength in the longitudinal direction is high compared to the transverse direction because of the high tensile strength of the fibres in the longitudinal direction.

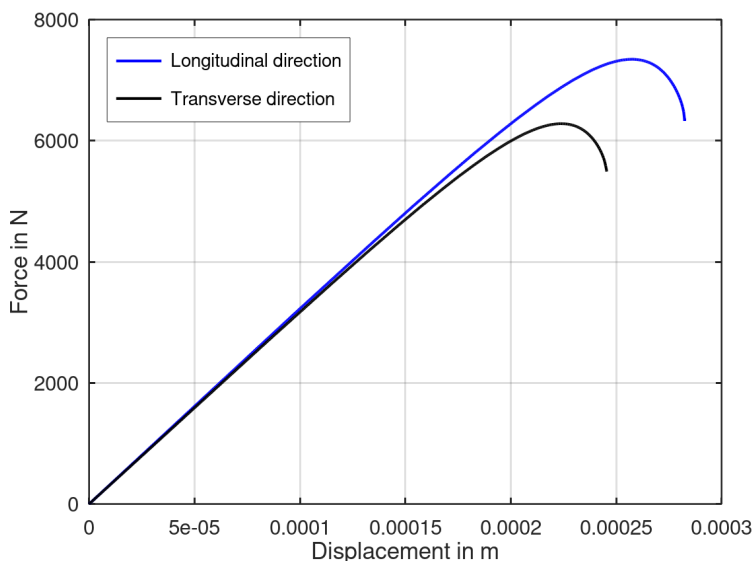


Figure 5.17: Comparison of force-displacement response in longitudinal and transverse direction for  $h=0.5\text{mm}$  discretization

### 5.3.2 Compact Tension (CT) Specimen

This second example will demonstrate the model's ability to calculate multiple damage variables simultaneously, i.e., to show the anisotropic damage development when a load is applied. In the Plane stress (2D) setting, the material is considered to be transversely isotropic; therefore, two damage variables ( $d_1$  and  $d_2$ ) are used to show the anisotropic damage development. The Compact Tension test is a standard test for plane fracture of materials and the measurement of fatigue crack growths. Because of the symmetry, only one half of the specimen is modelled, and the geometry and appropriate boundary conditions are given in the Figure (5.18). The mesh consists of plane stress (PLANE 182) elements with bilinear interpolations for displacements, and  $2 \times 2$  Gauss integration has been utilized. Just like the previous test, three different finite element meshes have been used in the fracture zone with the elements of size  $h=1\text{mm}$ ,  $0.5\text{mm}$  and  $0.25\text{mm}$  and a total of 509, 1409, 4811 elements respectively for the convergence studies (Figure 5.19). A node is created at the centre of the pinhole, and the innermost nodes of the pinhole contour are connected to this node by coupling option in ANSYS. A displacement controlled load ( $U_x$ ) is applied at the central node, and the global force-displacement response can be obtained from this central node. At first, the longitudinal direction is kept parallel to the loading direction, and the behaviour of the model is analyzed.

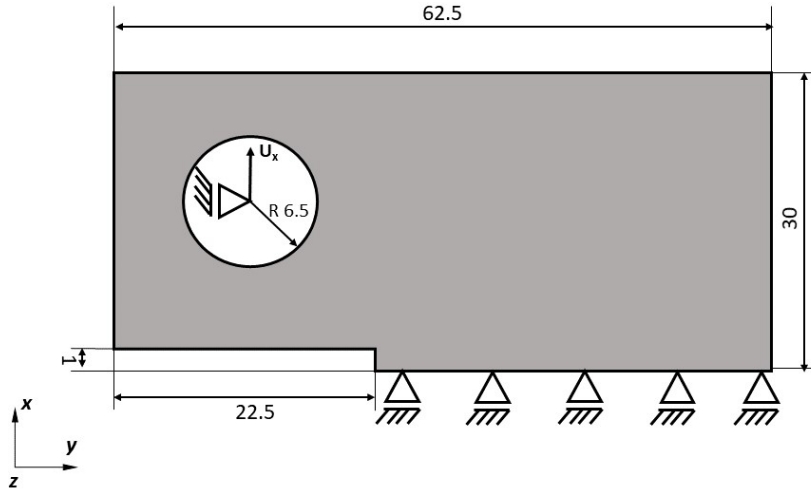
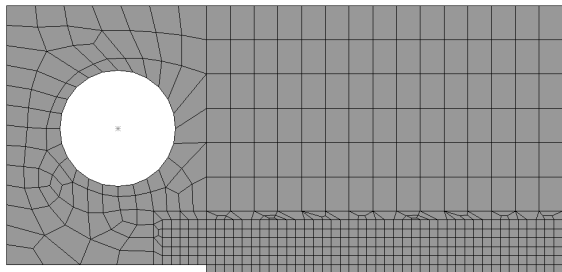


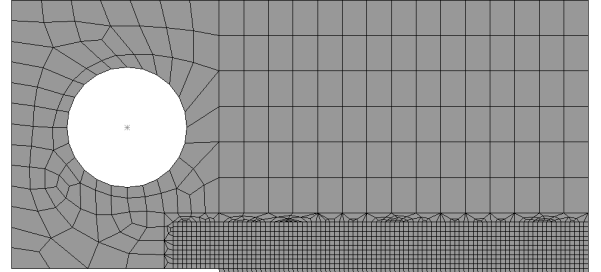
Figure 5.18: Specimen geometry and boundary conditions. Dimensions are given in mm. Displacement controlled loading  $U_x$  is applied

The global force-displacement response has been plotted for the three different meshes in the Figure (5.20). As expected, the maximum load capacity decreases slightly with the decrease in mesh size (or increase in the number of elements) because of the mesh dependence of the damage evolution law. The distributions of the damage variables  $d_1$  and  $d_2$  at the end of the loading process for the three different meshes

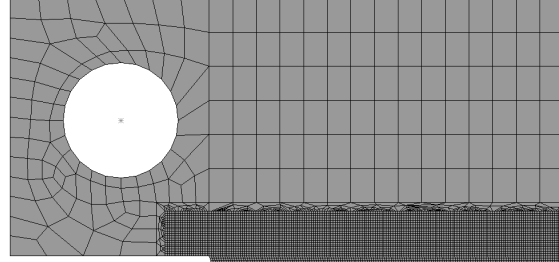
have been plotted in the Figure (5.21). The damage  $d_1$  is caused by tension in the longitudinal direction and  $d_2$  by tension in the transverse direction. A large portion of the fracture zone takes part in the damage process, and the width of the damage zone for  $d_1$  is approximately the same in the three discretizations. When damage  $d_1$  reaches the maximum threshold in almost all the damaged elements, the simulations comes to a stop; therefore, the maximum value and distribution of the damage variable  $d_2$  is dependant on the size of the element. From Figures (5.21b), (5.21d) and (5.21f) it is clearly evident that the maximum value and the width of the damage zone for  $d_2$  increases with decrease in mesh size.



(a)  $h=1\text{mm}$ ,  $n= 509$  elements



(b)  $h=0.5\text{mm}$ ,  $n= 1409$  elements



(c)  $h=0.25\text{mm}$ ,  $n= 4811$  elements

Figure 5.19: Considered meshes ( $h$  is the length of the element along fracture zone and  $n$  the total number of elements)

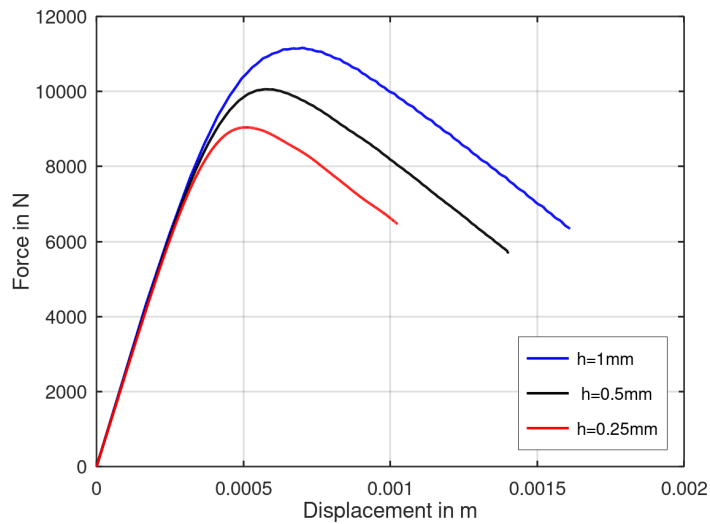
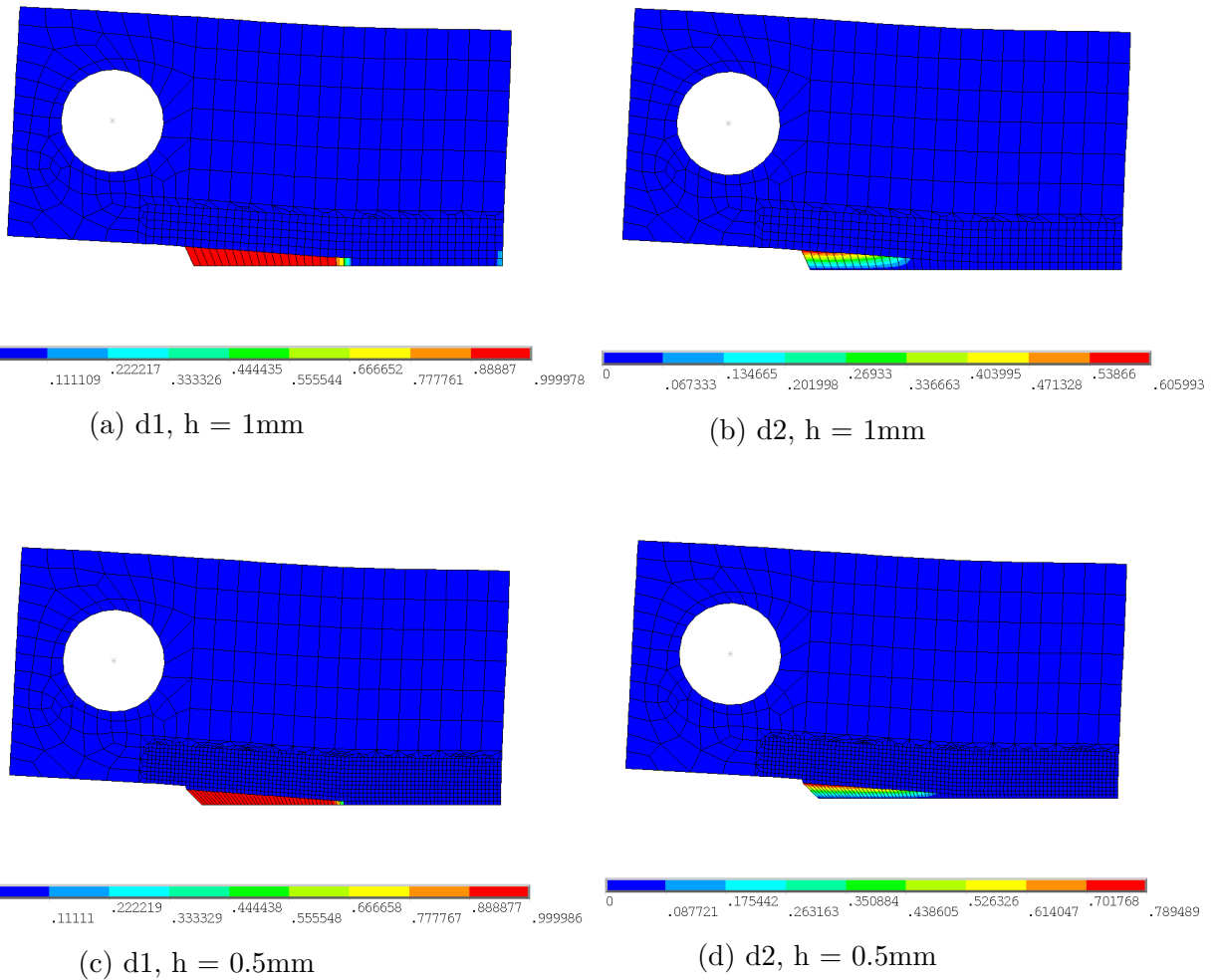
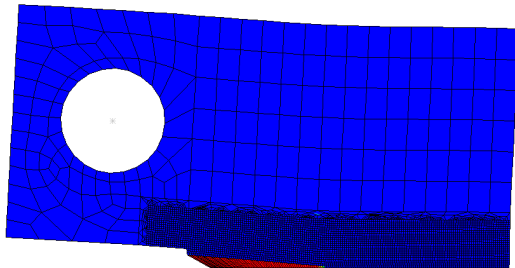
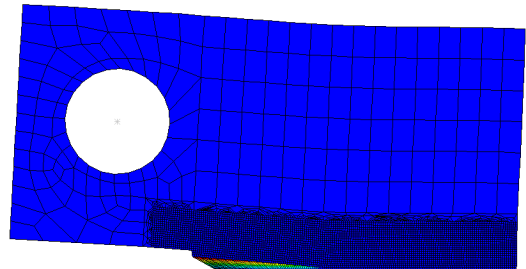


Figure 5.20: Convergence study: Global force-displacement response for three different meshes





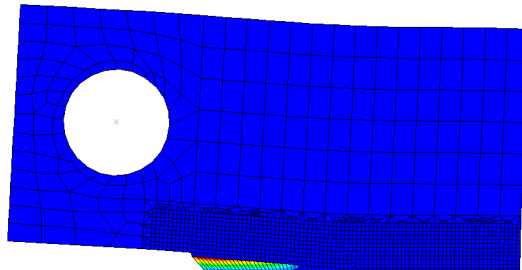
(e)  $d_1$ ,  $h = 0.25\text{mm}$



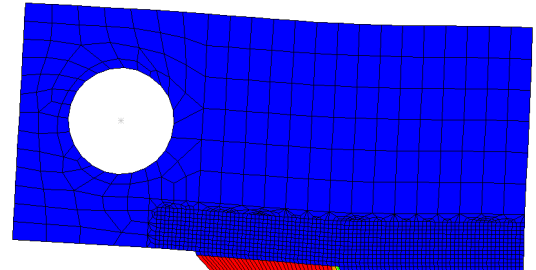
(f)  $d_2$ ,  $h = 0.25\text{mm}$

Figure 5.21: Damage distributions at the end of loading in longitudinal direction:  
Damage contour plots  $d_1$  and  $d_2$

Now the transverse direction is kept parallel to the loading direction, and the behaviour of the damage model, i.e., the anisotropic development of damage  $d_1$  and  $d_2$  is analysed. In this case, damage  $d_2$  is the primary damage variable and damage  $d_1$  is dependent on the mesh size. The damage distributions ( $d_1$  and  $d_2$ ) for loading in transverse direction and force-displacement comparison of longitudinal and transverse loading for  $h=0.5\text{mm}$  discretization are shown in the figure (5.22) and (5.23) respectively.



(a)  $d_1$



(b)  $d_2$

Figure 5.22: Damage distributions at the end of loading in transverse direction: Dam-  
age contour plots  $d_1$  and  $d_2$  ( $h = 0.5\text{mm}$  discretization)

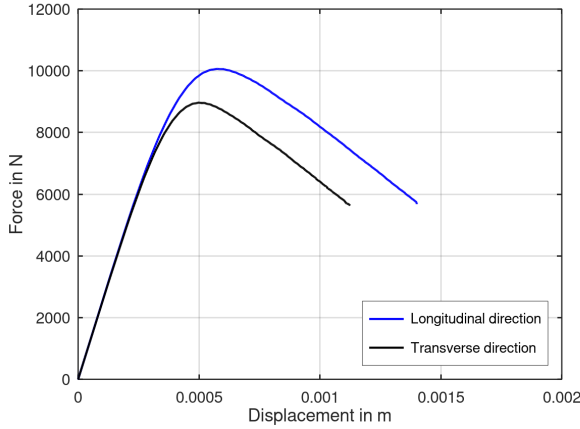


Figure 5.23: Comparison of force-displacement response in longitudinal and transverse direction for  $h=0.5\text{mm}$  discretization

### Effect of shear in damage development

To deeply understand the failure of composite materials, the effect of shear on damage initiation and propagation is studied. The effect of shear stress into each failure mechanism is introduced by the modified Hashin's failure criterion (Section (4.3.4)) where  $\alpha$  is the shear contribution factor which ranges from 0 to 1. The effect of shear can be studied by varying this shear contribution factor  $\alpha$ . The maximum value of  $\alpha$  is chosen to be 0.5 to avoid the damage development only due to shear because the shear strength is low compared to other strengths. The global force-displacement response for different  $\alpha$  by loading the CT-Specimen in the longitudinal direction is shown in the Figure (5.24) below. It is evident that by increasing  $\alpha$ , the failure index increases, which reduces the maximum load capacity of the CT specimen.

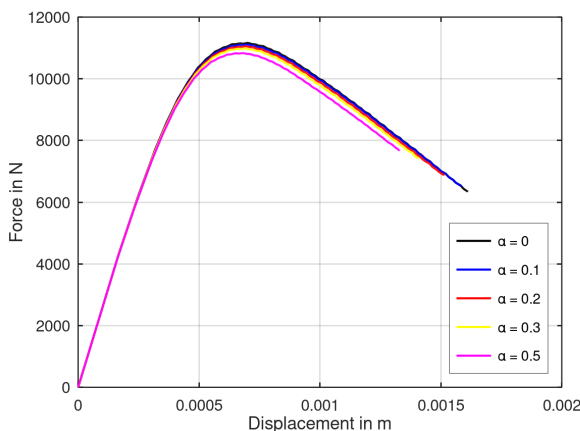


Figure 5.24: Comparison of force-displacement response for different shear co-efficient ( $\alpha$ ) ( $h=1\text{mm}$  discretization)

From the Figure (5.25), it is clear that the increase in shear contribution has little to no effect in the initiation and distribution of the damage  $d_1$  because the shear stress component ( $\sigma_{12}$ ) is very low compared to the stress in the longitudinal direction ( $\sigma_{11}$ ). However, the shear stress ( $\sigma_{12}$ ) affects the damage initiation and propagation of damage  $d_2$  because its magnitude is almost similar to the stress component ( $\sigma_{22}$ ) which was the only component responsible for damage  $d_2$  in case of the Maximum stress criterion previously utilized.

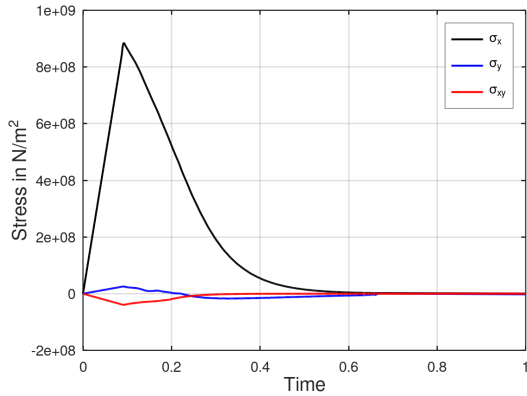
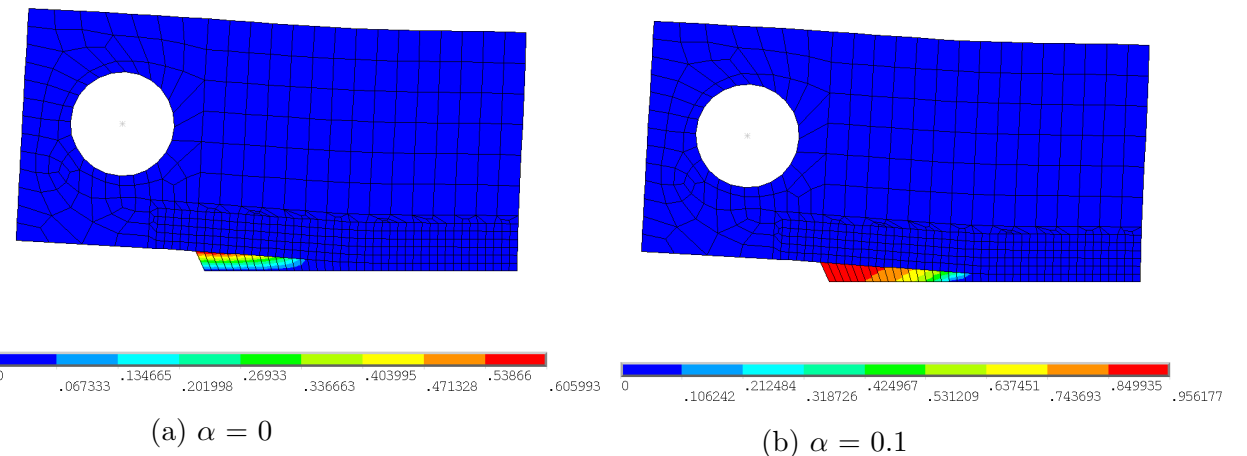
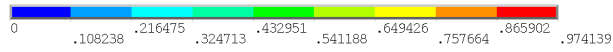
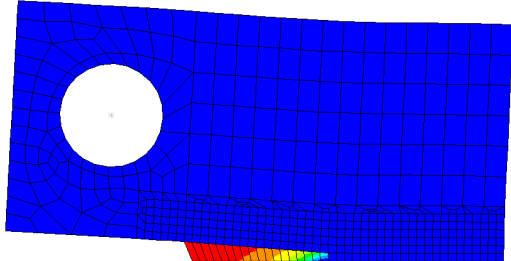


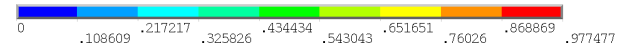
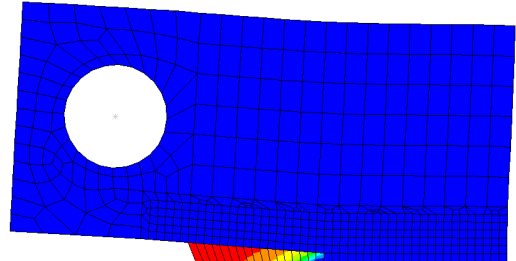
Figure 5.25: Evolution of stress components during longitudinal tensile loading ( $h=1\text{mm}$  discretization)

The contour plots of damage  $d_2$  for increasing shear contribution is plotted in the Figure (5.28). Compared to no shear effect ( $\alpha = 0$ ), the model with the presence of shear effect has more realistic damage propagation of ( $d_2$ ), and the width of the damage zone is significantly larger. For the model with shear effect, the width of the damage zone is almost similar in all the cases, but the maximum damage value and the number of elements reaching critical damage value increase with the increase in  $\alpha$ .

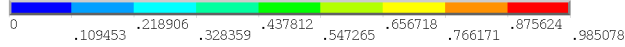
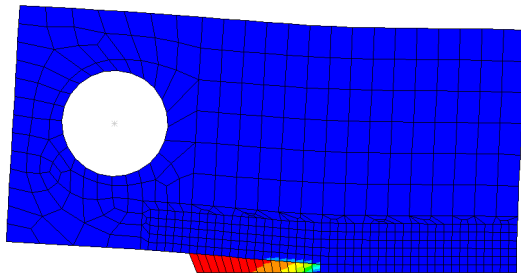




(a)  $\alpha = 0.2$



(b)  $\alpha = 0.3$



(a)  $\alpha = 0.5$

Figure 5.28: Damage distributions at the end of Longitudinal loading: Damage contour plots  $d_2$  for different shear co-efficient ( $\alpha$ )

In the case of transverse loading, the damage  $d_2$  is unaffected because the magnitude of the shear stress ( $\sigma_{12}$ ) is very low compared to the stress ( $\sigma_{22}$ ). However, the damage  $d_1$  is affected because the magnitude of the shear stress component ( $\sigma_{12}$ ) is similar compared to ( $\sigma_{11}$ ).

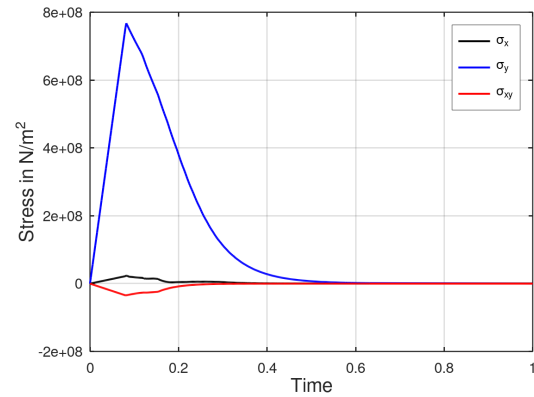


Figure 5.29: Evolution of stress components during transverse tensile loading ( $h=1\text{mm}$  discretization)

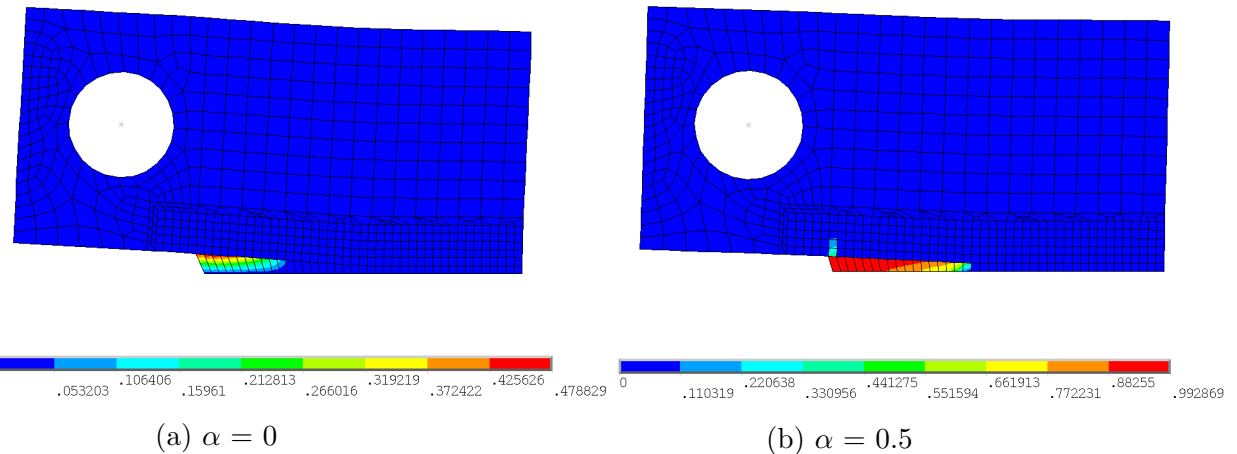


Figure 5.30: Damage distributions at the end of transverse loading: Damage contour plots  $d_1$  for different shear co-efficient ( $\alpha$ )

### 5.3.3 Plate with hole (3D)

This third example will demonstrate the model's ability to show the anisotropic damage development for three dimensional (3D) problems. In 3D, the material is considered to be orthotropic, so three damage variables ( $d_1$ ,  $d_2$  and  $d_3$ ) are used to show the anisotropic damage development, i.e., one damage variable for each principal material direction. Because of symmetry, only one-eighth of the specimen has been modelled. The geometry and the appropriate boundary conditions are given in the Figure (5.31). 8 node solid elements (SOLID 182) with trilinear interpolations of the displacements and full integration has been used to perform the FE modelling. The thickness was divided into four elements, and a very fine mesh has been used closer to the area of the fracture zone compared to other regions as shown in the Figure (5.32). At first, the longitudinal direction is kept parallel to the loading direction, and the behaviour of the model is analysed by applying displacement controlled load ( $U_x$ ) in the longitudinal direction (X-direction). Maximum stress criterion (4.3.2) has been used to predict the damage initiation in three principal material directions.

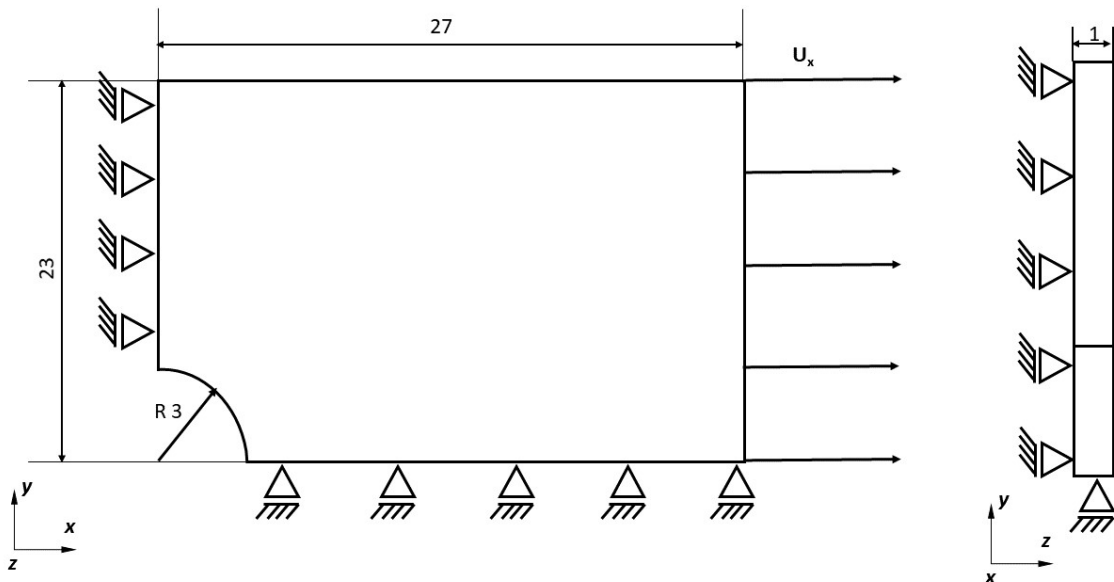


Figure 5.31: Specimen geometry and boundary conditions. Dimensions are given in mm. Displacement controlled loading  $U_x$  is applied

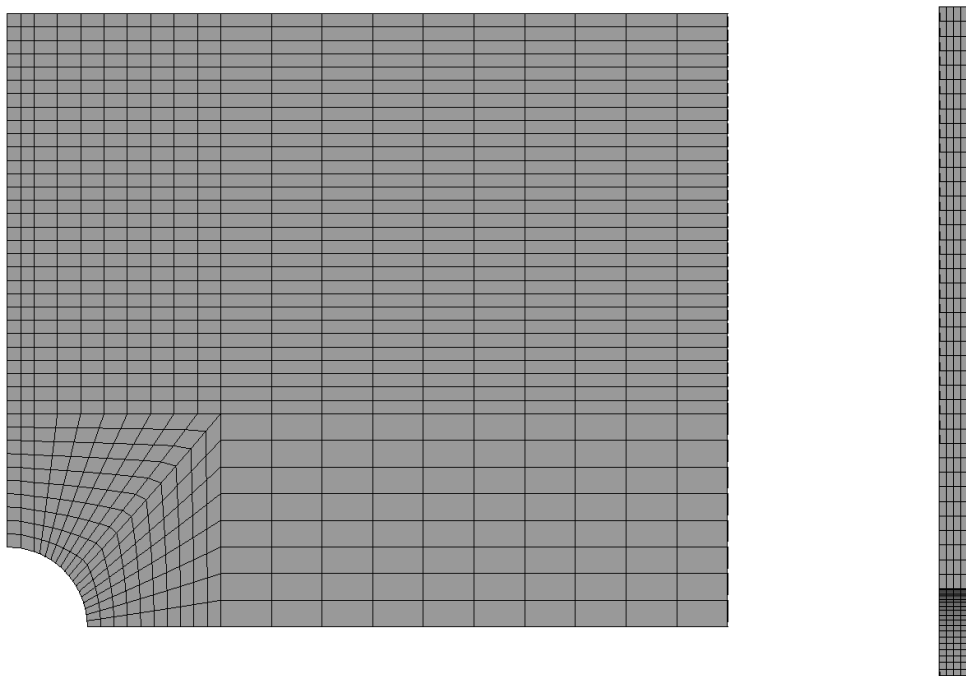


Figure 5.32: Finite element discretization used for 3D damage study

The global force-displacement response has been plotted for this longitudinal tensile loading in the Figure (5.33). The response is similar to the longitudinal loading in the notched tensile specimen, where it is characterized by a linear regime followed by a gradual drop of the load because of the softening.

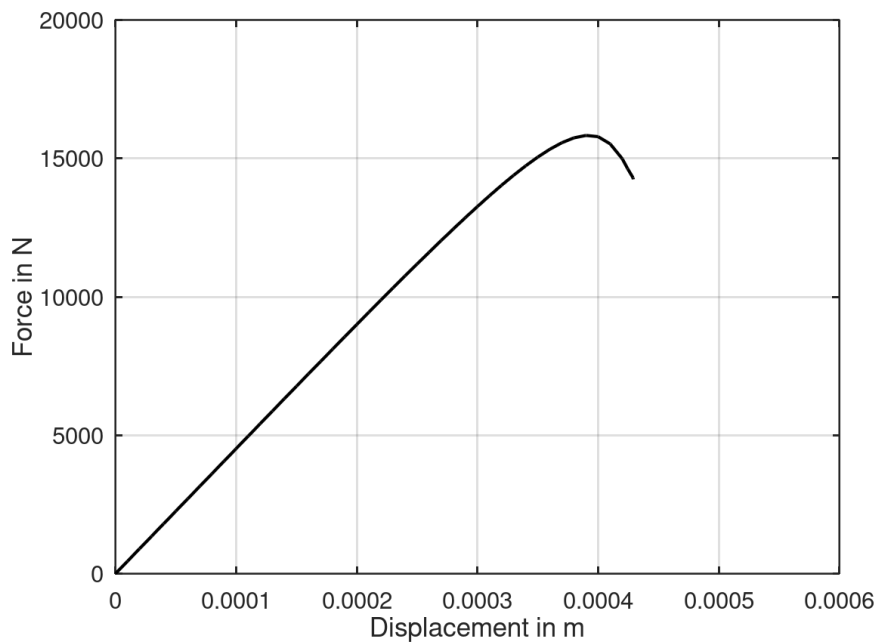
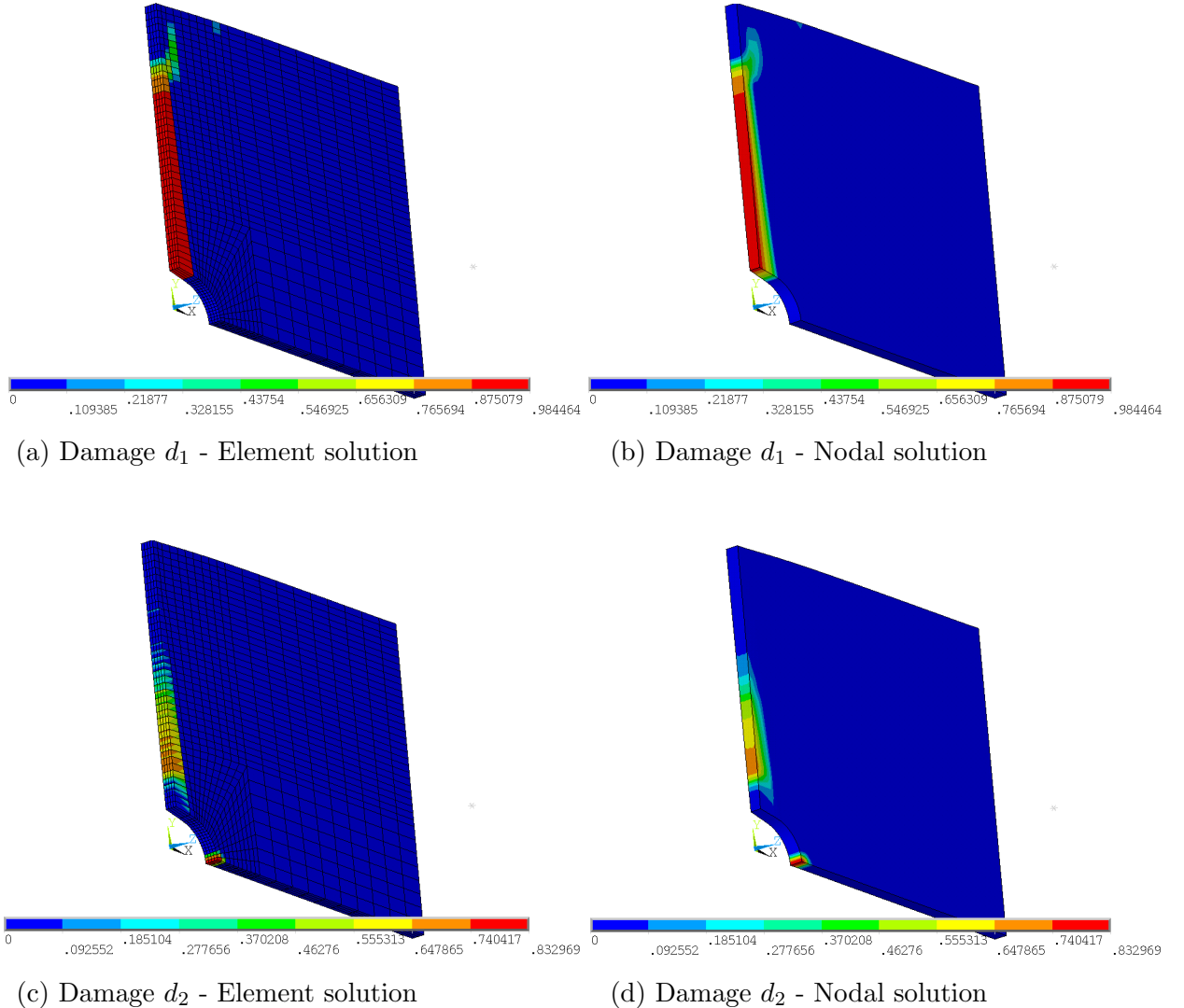


Figure 5.33: Global force-displacement response for the longitudinal tensile loading

The damage distribution ( $d_1$ ,  $d_2$  and  $d_3$ ) at the end of the tensile loading has been plotted in the Figure (5.34). In order to get a good visualization and understanding both elemental and nodal solution values of the damage has been plotted. The initiation and evolution of damage  $d_1$  is caused by the normal stress component  $\sigma_{11}$  in the longitudinal direction. The damage  $d_1$  initiates at the tip of the blunt notch and then propagates perpendicular to the loading direction. The evolution of damage  $d_2$  is caused by the normal stress component  $\sigma_{22}$  in the transverse direction. From figure (5.34c) and (5.34d) it is evident that the damage happens at two separate regions, i)perpendicular to the loading direction where damage  $d_1$  evolution already happened ii)right at the blunt notch at the bottom edge of the plate. It is observed that the damage  $d_2$  at the region (i) happens because of tension in the transverse direction, and in the region (ii), it is caused by the compression in the transverse direction. The propagation of damage  $d_2$  is caused by the normal stress component  $\sigma_{33}$  in the thickness direction



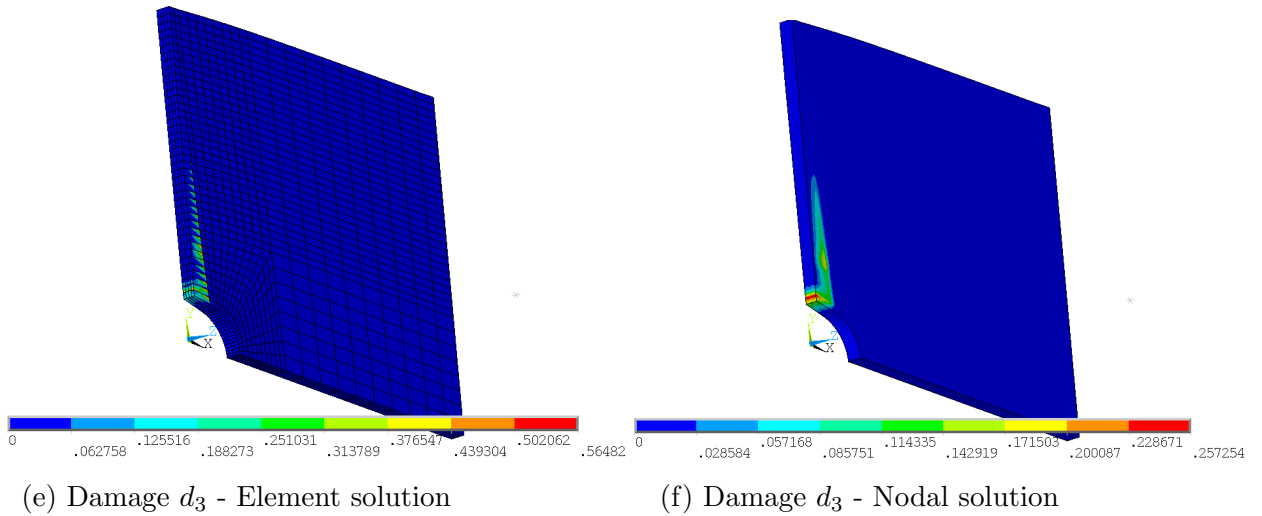
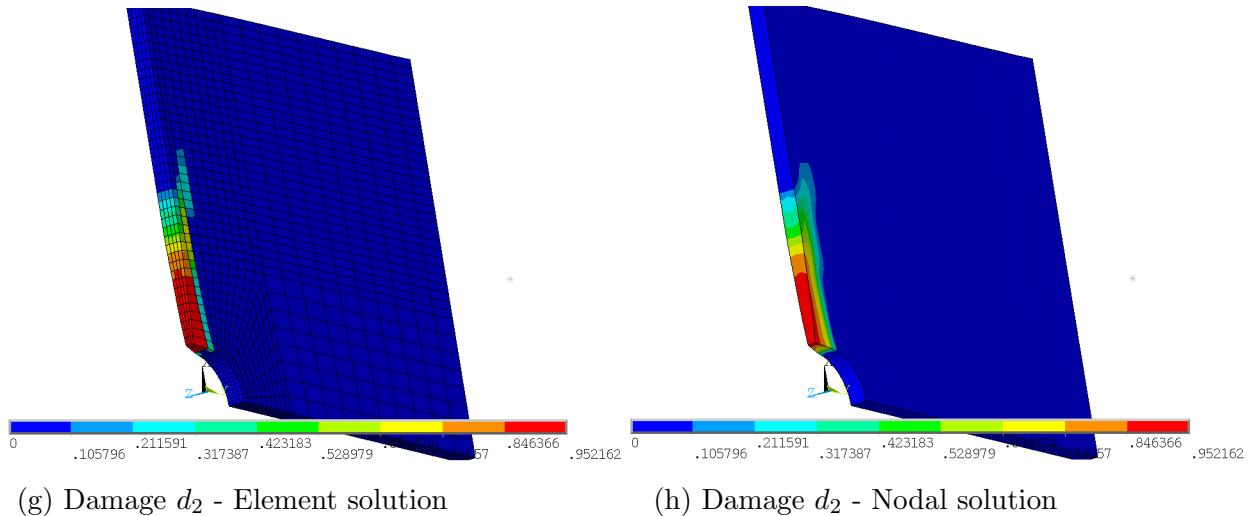


Figure 5.34: Contour plots of the damage distribution  $d_1$ ,  $d_2$  and  $d_3$  at the end of longitudinal tensile loading

Now the transverse direction is kept parallel to the loading direction, and the behaviour of the damage model, i.e., the anisotropic development of damage  $d_1$ ,  $d_2$  and  $d_3$  is analysed. Both tension and compression test has been carried out to see the difference in material behaviour.



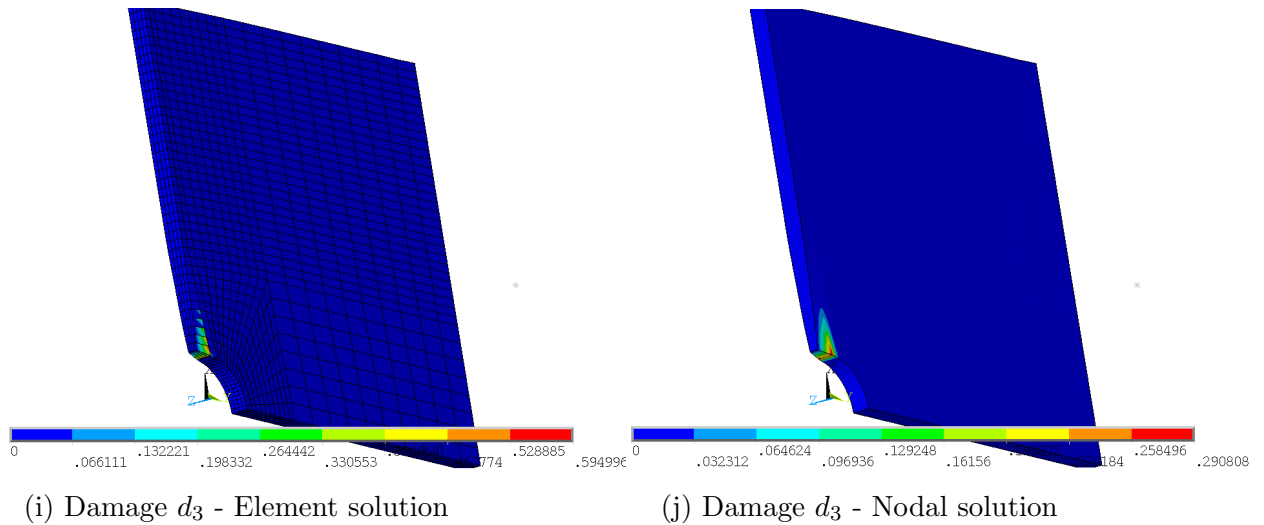
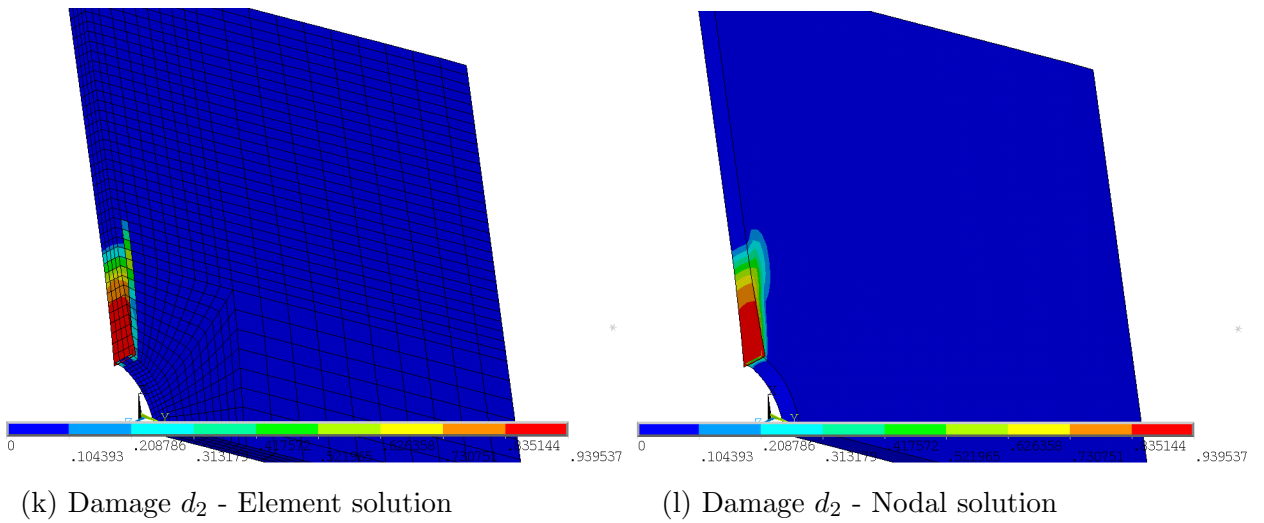


Figure 5.34: Contour plots of the damage distribution  $d_2$  and  $d_3$  at the end of transverse tensile loading



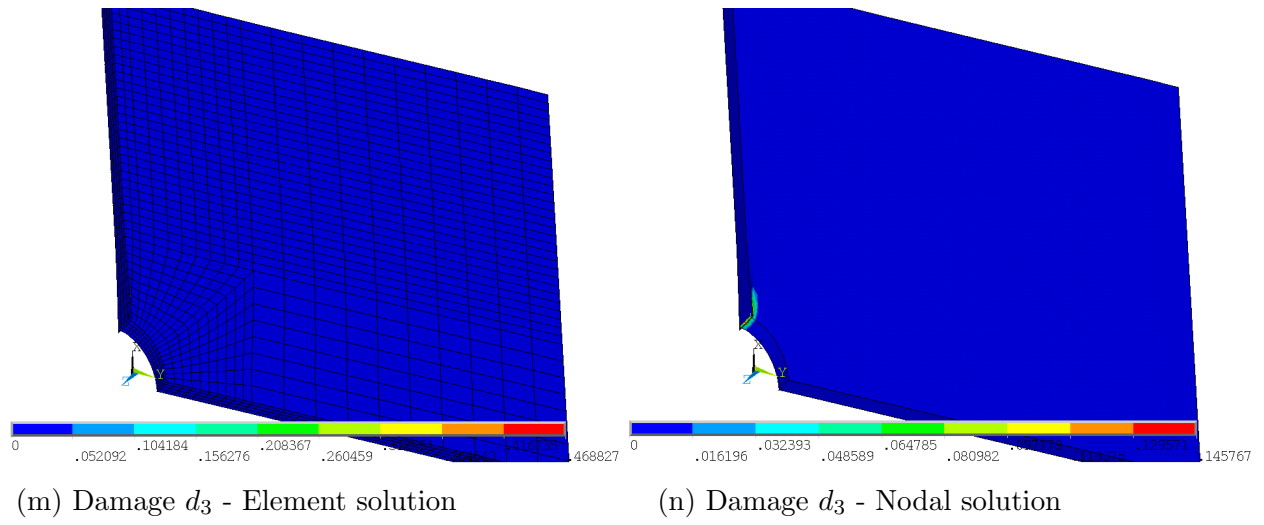


Figure 5.34: Contour plots of the damage distribution  $d_2$  and  $d_3$  at the end of transverse compressive loading